

NASA CONTRACTOR
REPORT

NASA CR-150577

SOLID PROPELLANT ROCKET MOTOR INTERNAL BALLISTICS
PERFORMANCE VARIATION ANALYSIS (PHASE THREE)

By Richard H. Sforzini, Winfred A. Foster, Jr., Jesse E. Murph,
and G. Wade Adams, Jr.
Auburn University
School of Engineering
Auburn, Alabama

November 1977

Final Report

(NASA-CR-150577) SOLID PROPELLANT ROCKET
MOTOR INTERNAL BALLISTICS PERFORMANCE
VARIATION ANALYSIS, PHASE 3 Final Report
(Auburn Univ.) 87 p HC A05/MF A01 CSCL 21H



Prepared for

NASA - George C. Marshall Space Flight Center
Marshall Space Flight Center, Alabama

TECHNICAL REPORT STANDARD TITLE PAGE

1. REPORT NO. NASA CR-150577	2. GOVERNMENT ACCESSION NO.	3. RECIPIENT'S CATALOG NO.	
4. TITLE AND SUBTITLE Solid Propellant Rocket Motor Internal Ballistics Performance Variation Analysis (Phase Three)		5. REPORT DATE November 1977	6. PERFORMING ORGANIZATION CODE
		8. PERFORMING ORGANIZATION REPORT NO.	
7. AUTHOR(S) Richard H. Sforzini and Winfred A. Foster, Jr., Jesse E. Murph and G. Wade Adams, Jr.		10. WORK UNIT NO.	
9. PERFORMING ORGANIZATION NAME AND ADDRESS Auburn University School of Engineering Auburn, Alabama		11. CONTRACT OR GRANT NO. NCA8-00120 and NCA8-00124	
		13. TYPE OF REPORT & PERIOD COVERED Contractor Report Final	
12. SPONSORING AGENCY NAME AND ADDRESS National Aeronautics and Space Administration Washington, D. C. 20546		14. SPONSORING AGENCY CODE	
		15. SUPPLEMENTARY NOTES Prepared under Modification No. 19 to the Cooperative Agreement, dated February 11, 1969, between Marshall Space Flight Center and Auburn University.	
13. ABSTRACT The report presents results of continued research aimed at improving the predictability of off-nominal internal ballistics performance of solid propellant rocket motors (SRMs) including thrust imbalance between two SRMs firing in parallel. The previous design analysis and Monte Carlo computer programs developed by the authors for use in such performance analyses are extensively revised to permit easier use and substantial reduction in computer operating time. An earlier analysis of internal ballistic effects of circular-perforated propellant grain deformation is verified by additional comparisons with test results. The potential effects of nozzle throat erosion on internal ballistic performance are studied and a new propellant burning rate law postulated. The propellant burning rate model when coupled with the grain deformation model permits an excellent match between theoretical results and test data for the Titan IIIC, TU455.02, and the first Space Shuttle SRM (DM-1). Analysis of star grain deformation using an experimental model and a finite element model shows the star grain deformation effects for the Space Shuttle to be small in comparison to those of the circular-perforated grain. An alternative technique is developed for predicting thrust imbalance without recourse to the Monte Carlo computer program. A scaling relationship used to relate theoretical results to test results may be applied to the alternative technique of predicting thrust imbalance or to the Monte Carlo evaluation. Extended investigation into the effect of strain rate on propellant burning rate leads to the conclusion that the thermoelastic effect is generally negligible for both steadily increasing pressure loads and oscillatory loads. The capability to calculate the influence of oscillating pressure loads on transient burning rates making use of the Zeldovich and Novozhilov transient burning rate model demonstrated during the course of this investigation may prove useful in combustion instability investigations.			
17. KEY WORDS		18. DISTRIBUTION STATEMENT Unclassified-Unlimited <i>A. A. McCoil</i> A. A. McCoil, Director Structures & Propulsion Laboratory	
19. SECURITY CLASSIF. (of this report) Unclassified	20. SECURITY CLASSIF. (of this page) Unclassified	21. NO. OF PAGES 89	22. PRICE NTIS

ACKNOWLEDGEMENTS

The authors express appreciation to personnel at the George C. Marshall Space Flight Center for their many useful suggestions which materially aided this investigation and in particular to Mr. B. W. Shackelford, Jr., NASA Project Coordinator, who additionally provided data for analysis and helpful encouragement to this research.

The participation of the following from the Aerospace Engineering Department at Auburn University is likewise acknowledged with appreciation: Mr. C. D. Evans, graduate research assistant, who constructed the model of the star grain, conducted the deformation tests, and assisted in evaluation of the results; Mr. J. L. Berry, laboratory assistant, who prepared a number of figures and assisted in computer programming and in obtaining computer results; and Mrs. M. N. McGee who typed the manuscript.

TABLE OF CONTENTS

List of Figures	v
List of Tables	viii
Nomenclature	ix
I. Introduction and Summary	1
II. Thrust Imbalance Predictions	4
Linear Approximation to Monte Carlo Imbalance Equations.	4
Comparison with Test Results	14
III. Improvement of Previous Computer Programs	21
Design Analysis Computer Program	21
Monte Carlo Computer Program	26
IV. Effects of Grain Deformation on Internal Ballistics.	30
Investigation of Nozzle Throat Variation	30
Burning Rate Model	34
Final Comparisons with Test Data	37
Deformation of Star Grains	41
Modification of the Deformation-Design Analysis Computer Program.	46
V. Thermomechanical Analysis	50
Propellant Modulus Model	50
Influence on Propellant Burn Rate Produced by Oscillating Pressure Loads	54

TABLE OF CONTENTS (Concluded)

Effects of Poisson's Ratio, Thermal Expansion and Thermal Conductivity	59
Effects of Mechanical Vibration on Motor Performance	64
Summary of Ignition Transient Analysis	67
VI. Concluding Remarks	71
References	72

LIST OF FIGURES

Fig. II-1.	Correlations determined from a set of 30 theoretical Titan IIIC SRM pairs obtained from a Monte Carlo evaluation.	5
Fig. II-2.	Correlations determined from a set of 30 theoretical Space Shuttle SRM pairs obtained from a Monte Carlo evaluation.	7
Fig. II-3.	Correlations determined from a set of 30 theoretical Space Shuttle SRM pairs obtained from a Monte Carlo evaluation using Titan burning rate variations.	9
Fig. II-4.	Comparison of Space Shuttle and Titan IIIC Monte Carlo evaluations demonstrating the effect on thrust imbalance correlations of variations of burning rate coefficient.	10
Fig. II-5.	Comparison of Space Shuttle and Titan IIIC Monte Carlo evaluations showing the effect of variations of burning rate coefficient on the thrust imbalance standard deviation correlations	12
Fig. II-6.	Tolerance limits for thrust imbalance of 30 theoretical Space Shuttle SRM pairs (Probability 0.90 for 99.7% of the distribution)	13
Fig. II-7.	Correlations determined from flight data obtained from a set of 20 Titan IIIC SRM pairs.	15
Fig. II-8.	Scaling of the Space Shuttle theoretical thrust imbalance correlation to establish the Space Shuttle flight prediction correlation	17
Fig. II-9.	Scaling of the Space Shuttle theoretical thrust imbalance standard deviation correlation to establish the Space Shuttle flight prediction correlation	18
Fig. II-10.	Tailoff thrust imbalance tolerance limits (Probability 0.90 for 99.7% of the distribution)	19
Fig. IV-1.	Variation in nozzle throat diameter with time	33

LIST OF FIGURES (CONT'D)

Fig. IV-2.	Comparison of test data for the TU-455.02 SRM with theoretical performance calculated using the modified flame height burning rate model	38
Fig. IV-3.	Comparison of test data for the TX 354-5 SRM with theoretical performance calculated using the modified flame height burning rate model.	39
Fig. IV-4.	Comparison of test data for the Space Shuttle SRM (DM-1) with theoretical performance calculated using the modified flame height burning rate model.	40
Fig. IV-5.	Test setup for determination of star grain perimeter changes under pressurization.	43
Fig. IV-6.	Superimposed tracings of enlarged photographs of subscale Space Shuttle star point model under 0 and 400 psig pressurization	44
Fig. V-1.	Relaxation modulus versus temperature	52
Fig. V-2.	Comparison of burning rate ratio for the constant propellant modulus model and relaxation modulus model . .	53
Fig. V-3.	Comparison of the results obtained for different pressurization rates.	55
Fig. V-4.	Results obtained for two oscillating pressure loads ($P_{av} = 200$ and 300 psia).	56
Fig. V-5.	Results obtained for two oscillating pressure loads ($P_{av} = 400$ and 500 psia).	57
Fig. V-6.	Results obtained for oscillating pressure load ($P_{av} = 500$ psia).	58
Fig. V-7.	Comparison of results obtained for two values of Poisson's ratio (Pressure = 50 sin (200 π t) + 500).	61
Fig. V-8.	Comparison of results obtained for two values of coefficients of thermal expansion (Pressure = 50 sin (200 π t) + 500)	62
Fig. V-9.	Comparison of results obtained for two different coefficients of thermal conductivity (Pressure = 50 sin (200 π t) + 500).	63
Fig. V-10.	Thrust versus time curves for various vibrational frequencies	66

LIST OF FIGURES (CONT'D)

Fig. V-11.	Comparison of the predicted ignition transients and test data for the Space Shuttle SRM	69
Fig. V-12.	Effect of increased flame-spreading speed on the predicted ignition transient for the Space Shuttle SRM	70

LIST OF TABLES

Table III-1	Sample input of multiple configurations for the design analysis computer program	23
Table III-2	Sample of partial output (I00=0) from the design analysis computer program	24
Table III-3	Sample of full output (I00=1) from the design analysis computer program, also showing ignition transient, propellant temperature distribution and inert weight results	25
Table III-4	Sample input for the Monte Carlo computer program	27
Table III-5	Sample output for the Monte Carlo computer program	28
Table IV-1	Sample input for the design analysis program with modifications for grain deformation and the modified burning rate model.	48
Table IV-2	Sample of partial output (I00=0) from the design analysis program with options for grain deformation effects (ISO=1) and modified burning rate model (IRO=2)	49

NOMENCLATURE

<u>English Symbol</u>	<u>Definition</u>	<u>Units Used</u>
a	Propellant burning rate coefficient.	in/sec-psi ⁿ
a _T	Time-temperature shift factor.	—
A	Cross-sectional area.	in ²
b	Average web-thickness of main propellant grain.	in.
c	Specific heat at constant volume.	in-lbf/lbm°R
c ₁	Constant giving ratio of peak amplitude of cyclic pressure loading to average pressure. Also, constant in the Summerfield burning rate law.	—, lbf-sec/in ³
c ₂	Constant in the Summerfield burning rate law.	lbf ^{1/3} -sec/in ^{5/3}
c ₃ , c ₄	Constants in modified burning rate law.	sec, (sec ³ /slug) ^{1/2}
C ₁ , C ₂	Constants in time-temperature shift factor (Eq. V-2).	—, °K
C _{F_o}	Ideal thrust coefficient.	—
CV	Coefficient of variation.	—
D	Thermoelastic energy dissipation.	°R/sec
E, E'	Modulus of elasticity and real part of the complex tensile modulus, respectively.	lbf/in ²
E _e , E _g	Modulus of elasticity under long-time steady loading conditions and at the glass transition temperature, respectively.	lbf/in ²
F	Thrust.	lbf
G	Mass flow rate per unit area.	slugs/sec-in ²
G'	Real part of the complex shear modulus.	lbf/in ²
K ₂	Two-sided statistical tolerance factor.	—
L, L _{ref}	Flow length and reference flow length, respectively, in modified flame height burning rate law.	in.

NOMENCLATURE (Continued)

<u>English Symbol</u>	<u>Definition</u>	<u>Units Used</u>
M	Mach number.	—
n	Burning rate exponent.	—
P	Pressure.	lbf/in ²
P _{cr}	Critical pressure in modified flame.	lbf/in ²
r	Burning rate.	in/sec
r ₀	Burning rate at zero velocity.	in/sec
Re	Reynolds number.	—
s	Standard deviation of a sample.	units vary
t	Time.	sec.
T	Absolute temperature	°R or °K
T _g	Glass transition temperature.	°K
u	Velocity parallel to the burning surface.	ft/sec
x _{Ta}	Difference in web thickness at ends of L _{Ta} (Ref. 5).	in.
\bar{X}	Value of general statistically distributed variable.	units vary
y	Distance burned.	in.
z	Instantaneous difference between web thickness at head and nozzle ends of controlling grain length, including any length associated with x _{Ta} and θ _G (Ref. 5).	in.
<u>Greek Symbol</u>		
α	Linear coefficient of thermal expansion.	1/°R
β, $\bar{\sigma}$	Shear loss and tensile loss modulus, respectively.	—

NOMENCLATURE (Continued)

<u>Greek Symbol</u>	<u>Definition</u>	<u>Units Used</u>
β_0	Constant exponent used in relaxation modulus expression.	—
γ	Ratio of specific heats.	—
Δ	Change or difference in quantity.	units vary
ϵ	Strain.	—
ζ_F	Thrust loss coefficient.	—
λ	Thermal conductivity.	in-lbf/in-sec °R
ν	Poisson's ratio.	—
ρ	Density.	lbm/in ³
σ	The standard deviation of a statistically distributed variable; i.e., the square root of the second moment about its mean value. Also peak value of oscillatory normal stress.	units vary lbf/in ²
τ	Web thickness. Also peak value of the oscillatory normal stress.	in-lbf/in ²
τ_w	Web thickness.	in.
τ_0	Time constant used in relaxation modulus expression.	sec.
ω	Cyclic frequency.	Hz

Subscripts

Definition

a	Ambient. Also burning rate coefficient.
av	Average or mean value.
e	Exit plane of nozzle.
h	Head end of grain.
n	Nozzle end of grain at position of maximum flow Mach number.

NOMENCLATURE (Concluded)

Subscripts

Definition

N	Value for new motor.
c	Stagnation.
S	Space Shuttle.
SA	Adjusted value for Space Shuttle.
ss	Steady state.
t	Transient.
T	Titan IIIC.

Superscripts

·	Time rate of change of a quantity.
'	Experimental data.
*	Value of a variable where $M=1$.
-	Average or mean value.

I. INTRODUCTION AND SUMMARY

This report presents the results of research performed at Auburn University during the period November 19, 1976, to November 18, 1977, under Modification No. 19 to the Cooperative Agreement, dated February 11, 1969, between NASA Marshall Space Flight Center (MSFC) and Auburn University. The principal objective of the research is to further develop techniques for theoretical assessment of solid rocket motor (SRM) internal ballistic performance to include statistical investigation of thrust imbalance of pairs of SRMs firing in parallel as on the booster stage of the Space Shuttle.

The theoretical thrust imbalance of SRM pairs has been previously investigated statistically using a Monte Carlo technique (Ref. 1-4). The results of this investigation include a computer program which selects sets of significant variables on a probability basis and calculates the performance characteristics for a large number of motor pairs using a mathematical model of the internal ballistics. This model is based on an earlier basic computer program (Refs. 5 and 6) which permits rapid assessment of internal ballistic performance using simplifying assumptions which have been demonstrated to give realistic results. The basic program is known as the design analysis program. A complete listing of the design analysis program is given in Ref. 3. A few minor modifications are identified in Ref. 2. Reference 2 also lists the complete program with a special option which permits assessment of the effects of circular-perforated grain deformation on internal ballistics. As adopted into the Monte Carlo program, the basic design analysis program does not include the grain deformation analysis but does include an analysis which accounts for the effects of propellant grain out-of-roundness, eccentricity and/or nonaxisymmetric grain temperature distribution. A listing of the complete Monte Carlo program is also given in Ref. 3 with a few minor improvements identified in Ref. 2.

The research which culminated in the development of the design analysis and Monte Carlo programs revealed a number of areas in which the programs may be improved. Also, an alternative scheme for predicting thrust imbalance has been suggested, and the methods of assessing grain deformation and its ballistic effects need further verification. The extended research discussed in this report deals in part with such additional aspects.

During development of the Monte Carlo program the effects of strain rate on the performance of SRMs were examined (Refs. 2-3). The investigation disclosed that modification of the solid phase grain temperature distribution and hence propellant burning rate due to thermoelastic coupling may occur when strain rates are high; i.e., during highly transient conditions of operation. Although an assessment of single SRMs under ignition-

type pressure loads showed the burning rate effect is small, additional research was indicated with respect to effects of physical properties. Also, the thermoelastic effect needed to be evaluated under cyclic loading conditions such as those produced by oscillatory burning and mechanically induced vibrations. The extended research also embraces investigation of these areas.

The alternative scheme for predicting thrust imbalance that resulted from the extended research makes use of a demonstrated linear relationship between thrust imbalance at various times and the corresponding slopes of the nominal thrust-time trace for both theoretical (Monte Carlo) results and test data. A method is presented whereby the thrust imbalance of a new SRM design may be predicted from the linear relationship without recourse to a Monte Carlo analysis. The accuracy of the prediction is expected to be best during the tailoff portion of the trace. The method is restricted to SRMs employing similar manufacturing and processing controls to those of the Titan IIIC SRMs which constitute the baseline analysis. An exception is propellant burning rate variability which may be different for the new design since it is accounted for in the relationship. A scaling relationship is used to relate theoretical results to test results. This scaling relationship may be applied either to the alternative technique of predicting thrust imbalance or as an adjustment to a Monte Carlo analysis of thrust imbalance.

Improvements to the basic design and Monte Carlo computer programs are made in the following areas: 1) Modification of the input procedure in the programs to allow the use of NAMELIST for nonstatistical input variables. This simplifies the mechanics of card input for both programs and reduces the amount of input required for multiple configurations in the design analysis program. 2) Incorporation of an output option in the design analysis program which allows selection of a limited number of output variables greatly reducing the number of printed sheets and computer execution time. 3) Reduction in the volume of printed output in the Monte Carlo program by changes in the present format structure. This change causes all input data for each SRM to be written on a single page. 4) Modification of program logic and statement structure in both programs to decrease computational time and hence further increase program efficiency. The net result of all the changes is a reduction of typical computational times in the basic design program by approximately 40 percent for the limited output option and 20 percent for the full output. Monte Carlo program operational times are reduced by approximately 20 percent.

Attempts to further verify the influence of grain deformation on internal ballistics were impeded by the anomalous performance of the motor selected for the investigation. Efforts to explain the irregular behavior include analysis of nozzle throat behavior and propellant erosive burning characteristics. A new model of erosive burning, termed the modified flame height model, is developed which when combined with the grain deformation model permits excellent representation of the performance of the Castor TX354-5 and TU-455.02 SRMs. The model uses two constants which were selected for each motor to match test performance. The same constants used for the

TU-455.02 also gave a good match when used to predict the performance of the first Space Shuttle SRM (DM-1) which has a very similar, although not identical, propellant formulation. The new burning rate model was incorporated as an option into the same version of the design analysis program that contains the grain deformation analysis along with the other design analysis program improvements outlined above. Although this research provides additional evidence of the validity of the grain deformation analysis for circular-perforated grains, we feel that a sufficiently firm basis has not yet been established to warrant incorporating the analysis into the Monte Carlo program.

With the objective of finding a simplified approach to including the effects of star-type grain deformation into the program, an experimental subscale inert model of the Space Shuttle star grain segment was constructed. Perimeter changes measured under hydraulic pressure were approximately 0.2 percent at 400 psia. This was confirmed by a finite element analysis. The potential amount of burning perimeter change involved was judged to be small enough in comparison to circular-perforated changes (4.0 percent at 800 psi) to be considered negligible in the Space Shuttle. However, for grains with thicker webs and shorter star points the deformation is expected to be more substantial.

Additional investigation into the effect of propellant strain rate on propellant burning rate leads to the conclusion that for all practical purposes the effect is negligible for both steadily increasing pressure loads and oscillatory loads. The investigation includes incorporation of a relaxation modulus into the thermoelastic analysis and examination of the effect of Poisson's ratio, thermal expansion and thermal conductivity. A brief analysis of the effects of mechanical vibration on burning rate and internal ballistic performance as caused by the thermomechanical energy dissipation associated with viscoelastic materials is also included. An important by-product of this research is the demonstrated capability to calculate the influence of oscillating pressure loads (with or without thermoelastic coupling) on transient burning rates making use of the Zeldovich and Novozhilov (Z-N) transient burning rate model (Refs. 2 and 7). This analysis may prove useful for combustion instability studies irrespective of the thermoelastic effect. Likewise, an internal ballistic model of the ignition transients in SRMs also including the Z-N burning rate model developed in a separate effort (Ref. 8) under the general guidance of this project may prove of some utility.

As well as a general discussion of the changes that have been made to the basic computer programs, the text contains a detailed description of the new input formats for the design analysis and Monte Carlo programs and for the design analysis program with grain deformation and burning rate model options. Sample outputs are also presented for the three programs.

II. THRUST IMBALANCE PREDICTIONS

In Ref. 2, a statistical relationship is shown to exist between the thrust imbalance at various times and the corresponding slope of the nominal thrust-time trace for 30 theoretical Titan IIIC SRM pairs obtained from a Monte Carlo evaluation. The purpose of the present analysis is to refine and extend the investigations and conclusions of Ref. 2. More specifically, the new analysis establishes procedures for predicting the thrust imbalance trace for a new SRM pair directly from the slope of the nominal thrust-time trace without a Monte Carlo evaluation. Also, a scaling law is developed based on differences between the Monte Carlo evaluation and known test results for the Titan IIIC.

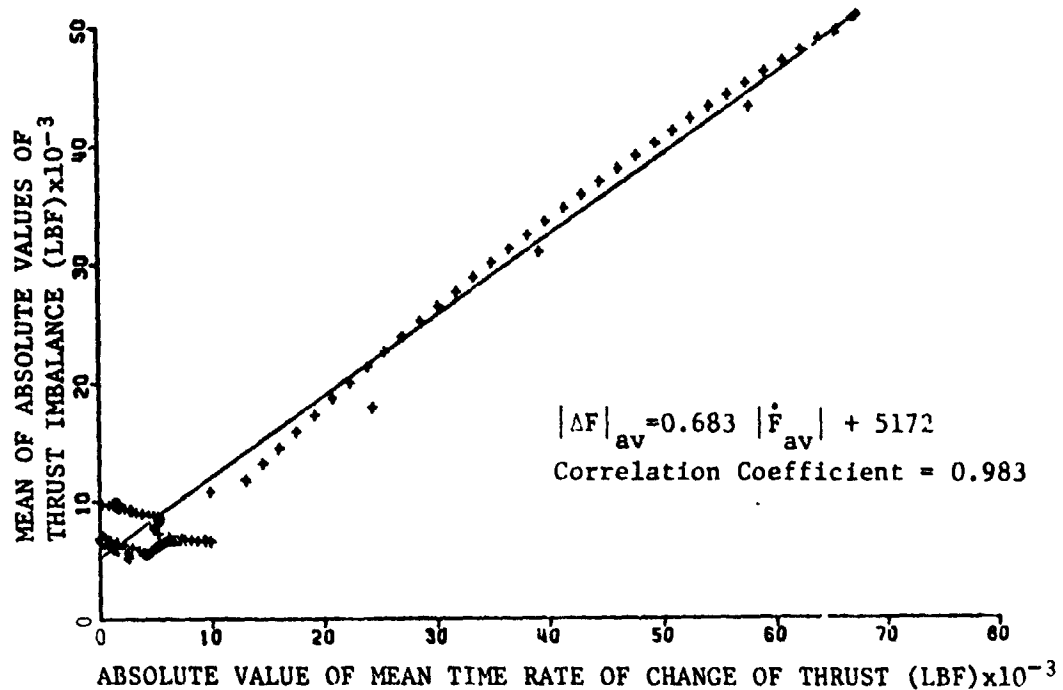
Linear Approximation to Monte Carlo Imbalance Equations

A question was raised in Ref. 2 concerning the randomness of selection of the time slices on which the thrust imbalance relationship was based. A rigorous statistical analysis of the relationship between the thrust imbalance and the thrust-time slope requires that a random selection of slopes be made, i.e., with no prior knowledge of thrust imbalance values. This necessitates a special search procedure since for a given value of thrust-time slope, several corresponding thrust imbalance values (at various times) may be found. The task becomes exceedingly complicated with relatively low values of thrust-time slope, especially when examining erratic test data.

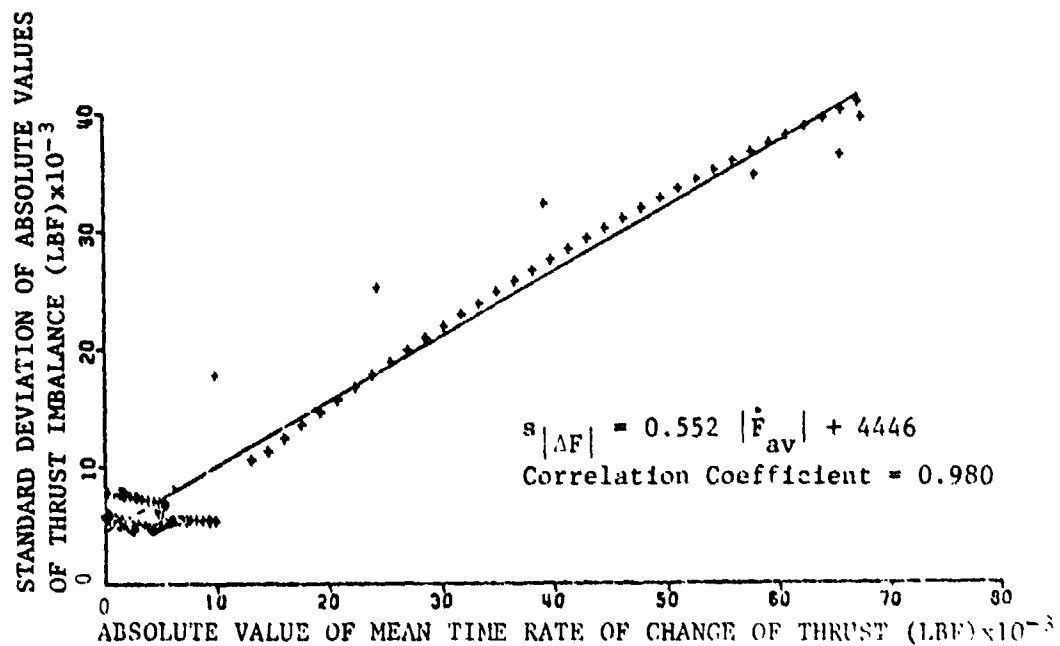
An alternative approach is to divide the thrust trace into a large number of equi-spaced time slices. While this does not represent a truly random selection of thrust-time slopes, it can be argued that the slopes are chosen with no prior knowledge of the thrust imbalance values. Although not completely rigorous, this procedure provides an accurate and consistent method of analyzing and predicting thrust imbalance, as will be demonstrated.

The alternative approach is applied to a set of 30 theoretical Titan IIIC SRM pairs. Time slices of motor pair imbalance traces and individual motor thrust traces are taken at 0.5 sec. increments throughout burn time, including tailoff. Average values of absolute thrust imbalance for the 30 pairs at each time slice are plotted versus the absolute values of the average thrust-time slopes for the 60 motors. This is shown in Fig. II-1a along with a linear least-squares approximation, $|AF|_{av} = 0.683|\dot{F}_{av}| + 5172$. A correlation coefficient, which indicates the accuracy of the linear approximation, is determined to be 0.983. These values agree very well with those presented in Ref. 2.

It should be noted here that relatively large values of thrust-time slope and thrust imbalance are experienced only during the tailoff period. Thus the slope of the linear approximation is determined principally by the tailoff characteristics, and the maximum value of thrust imbalance



a. Thrust imbalance vs. thrust-time slope



b. Standard deviation of thrust imbalance vs. thrust-time slope.

Figure II-1. Correlations determined from a set of 30 theoretical Titan IIIC SRM pairs obtained from a Monte Carlo evaluation.

occurs during the tailoff period. This observation tends to support the validity of using equi-spaced time slices in place of random values of thrust-time slope since the inherent, additional quantity of lower valued thrust-time slopes, obtained in the equi-spaced time slice method, only confirms the thrust imbalance intercept, and has little effect on the slope of the established relationship between thrust imbalance and thrust-time slope.

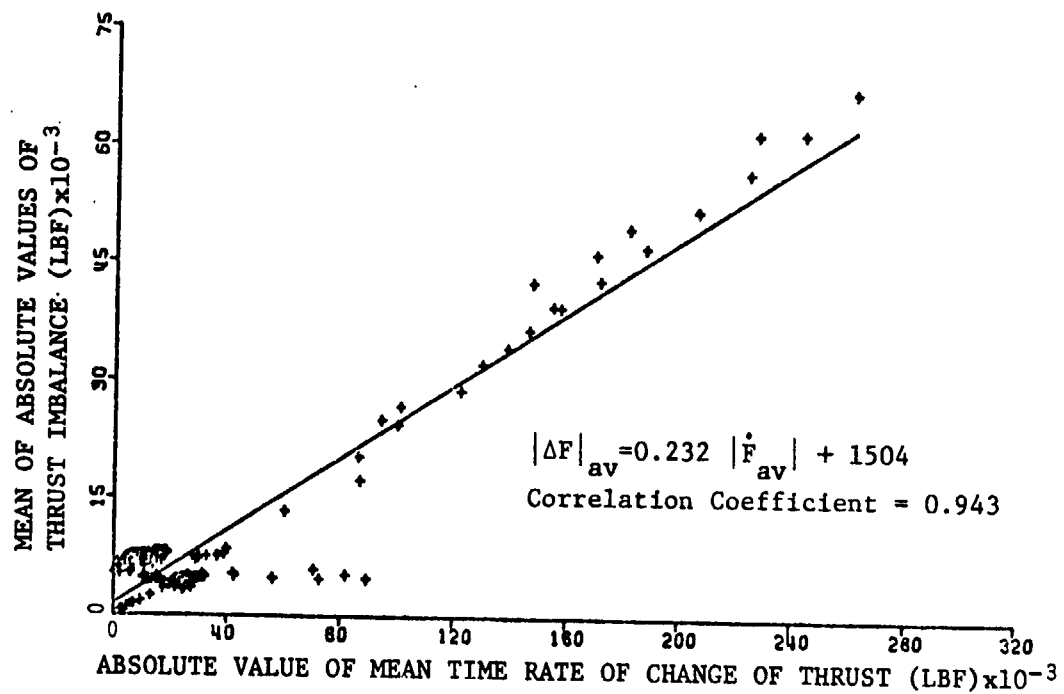
It is desired to compare this analysis of 30 theoretical Titan IIIC SRM pairs to an analysis of 30 theoretical Space Shuttle SRM pairs. After obtaining the latter SRM pairs from a Monte Carlo evaluation, the procedure described above is used to determine the thrust imbalance versus thrust-time slope correlations presented in Figure II-2a, with a linear least-squares approximation, $|\Delta F|_{av} = 0.232 |\dot{F}_{av}| + 1504$, and a correlation coefficient of 0.943. It is immediately obvious that the linear approximations for the two analyses are in considerable disagreement, which might well be expected when comparing two entirely different families of motors. It should be noted that the Space Shuttle SRM configuration used in the analysis differs somewhat from that used in Ref. 3 and includes changes that reduce tailoff thrust imbalance. The earlier configuration would exhibit higher thrust imbalances at correspondingly higher nominal thrust-time slopes. These sets of values would presumably lie close to an extension of the regression line on Fig. II-2a.

In examining the cause of the apparent discrepancy between the Titan and Space Shuttle SRM evaluations, it is advantageous to consider the sources of the data used; namely, the Monte Carlo evaluations, which use statistical data for determining variations of certain parameters. An examination of the statistical variations (standard deviations) of these parameters and their relative influences reveals that the variation of the burning rate coefficient may represent the most significant difference between the two analyses.

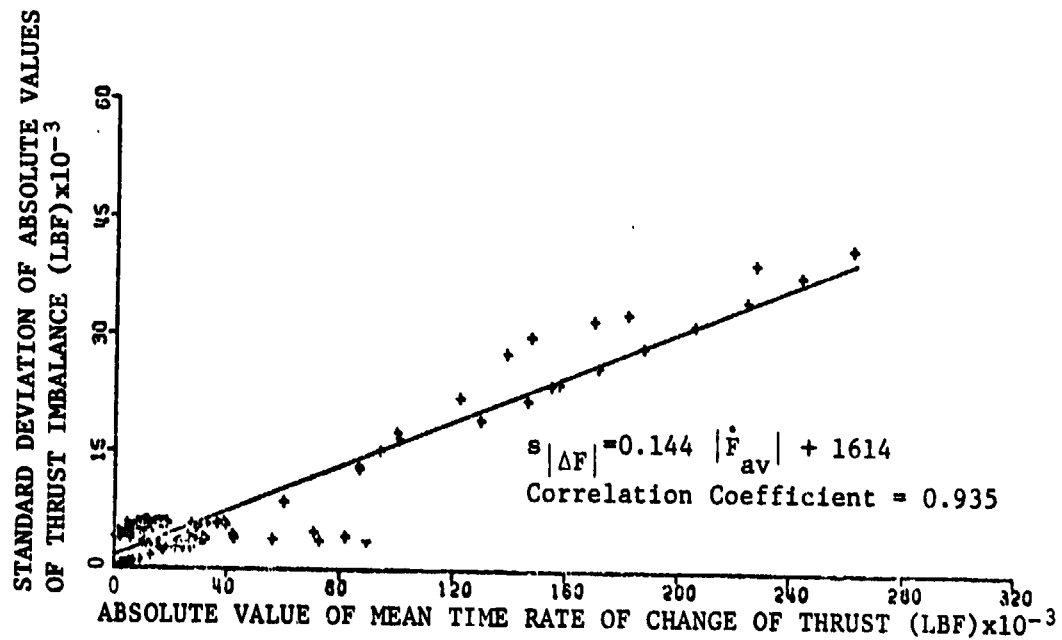
The other statistically varying parameters were found to have small influences on the thrust imbalance relationships because of similar coefficients of variation (standard deviation divided by mean value) for these two SRMs. Other SRMs might exhibit different variations of parameters and the effects could become influential.

The coefficient of variation of the Titan burning rate coefficient used in the analysis is

$$CV_T = \sigma_{a_T} / \bar{a}_T = 0.0003428 / 0.06653 = 0.005153. \quad (II-1)$$



a. Thrust imbalance vs. thrust-time slope.



b. Standard deviation of thrust imbalance vs. thrust-time slope.

Figure II-2. Correlations determined from a set of 30 theoretical Space Shuttle SRM pairs obtained from a Monte Carlo evaluation.

The coefficient of variation of the Space Shuttle burning rate coefficient used in the analysis is

$$CV_S = \sigma_{a_S} / \bar{a}_S = 0.000008335 / 0.006915 = 0.001205. \quad (II-2)$$

And, since the magnitudes of thrust imbalance result primarily from the variations of web-action times, not only should the variations in burning rate coefficients be examined, but also the web thicknesses. The coefficient of variation for the Space Shuttle burning rate coefficient may now be adjusted to that used for the Titan, including web thickness adjustment:

$$CV_{SA} = \tau_T CV_T / \tau_S = (36.16 \text{ in})(0.005153) / (460 \text{ in}) = 0.004589. \quad (II-3)$$

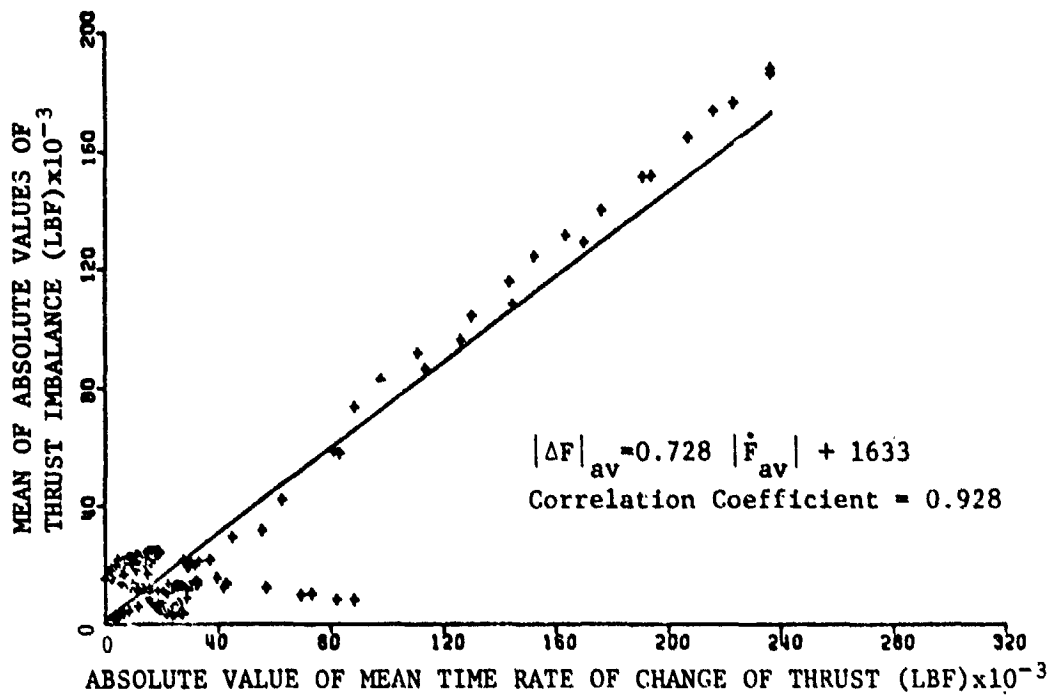
The adjusted Space Shuttle standard deviation is

$$\sigma_{a_{SA}} = \bar{a}_S CV_{SA} = (0.006915)(0.004589) = 0.00003173. \quad (II-4)$$

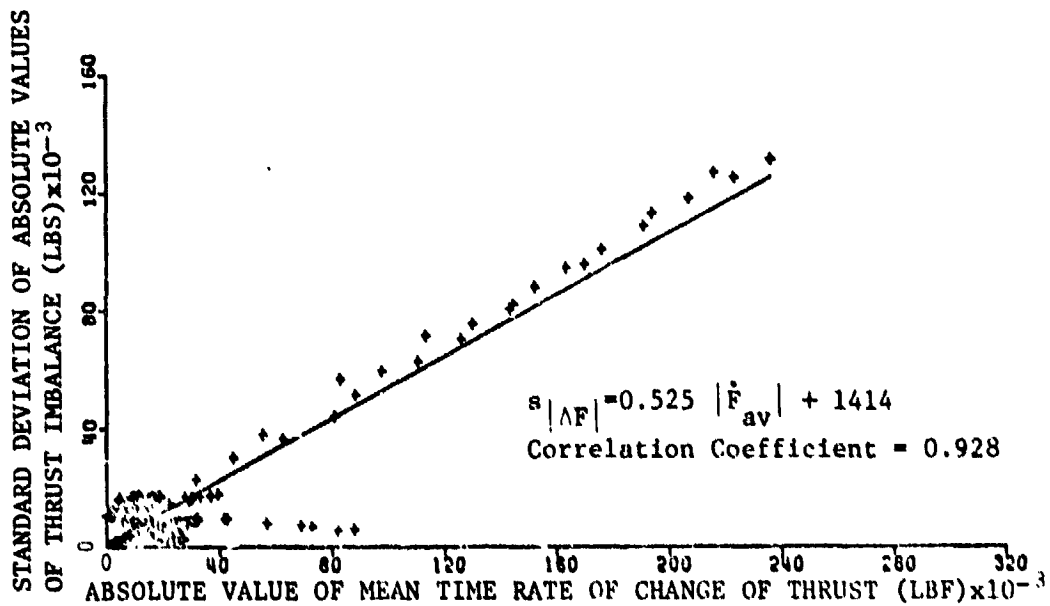
Using this adjusted value of statistical variation for the Space Shuttle burning rate coefficient, a Monte Carlo evaluation of 30 theoretical SRM pairs is obtained. Repeating the previously described time slice analysis results in the relationship of Fig. II-3a, with a linear approximation, $|\Delta F|_{av} = 0.728 |\dot{F}_{av}| + 1633$, and a correlation coefficient of 0.928. The effect of this burning rate adjustment is clearly seen when compared, as in Fig. II-4, to the original Space Shuttle and Titan analyses. It is noted that the Space Shuttle configuration with adjusted burning rate variations closely defines the thrust imbalance versus thrust-time slope of the theoretical Titan motors. Thus it is concluded that the burning rate coefficient and web thickness are the most significant factors influencing the magnitudes of the thrust imbalance, particularly during the tailoff period.

It now appears feasible that a thrust imbalance versus thrust-time slope relationship, based on a Monte Carlo evaluation, can be predicted for a pair of new motors firing in parallel or a family of new motors, without actually performing the Monte Carlo evaluation. However, this does require that the new motors have similar manufacturing tolerances and statistical variations (similar technology) on the significant motor parameters. Using both the Titan and Space Shuttle analyses as a base, a thrust imbalance relationship is determined for the new motors,

$$|\Delta F|_{av} = (0.0714 + 3.282 CV_N \tau_N) |\dot{F}_{av}| + (198 + 26,694 CV_N \tau_N), \quad (II-5)$$



a. Thrust imbalance vs. thrust-time slope.



b. Standard deviation of thrust imbalance vs. thrust-time slope.

Figure II-3. Correlations determined from a set of 30 theoretical Space Shuttle SRM pairs obtained from a Monte Carlo evaluation using Titan burning rate variations.

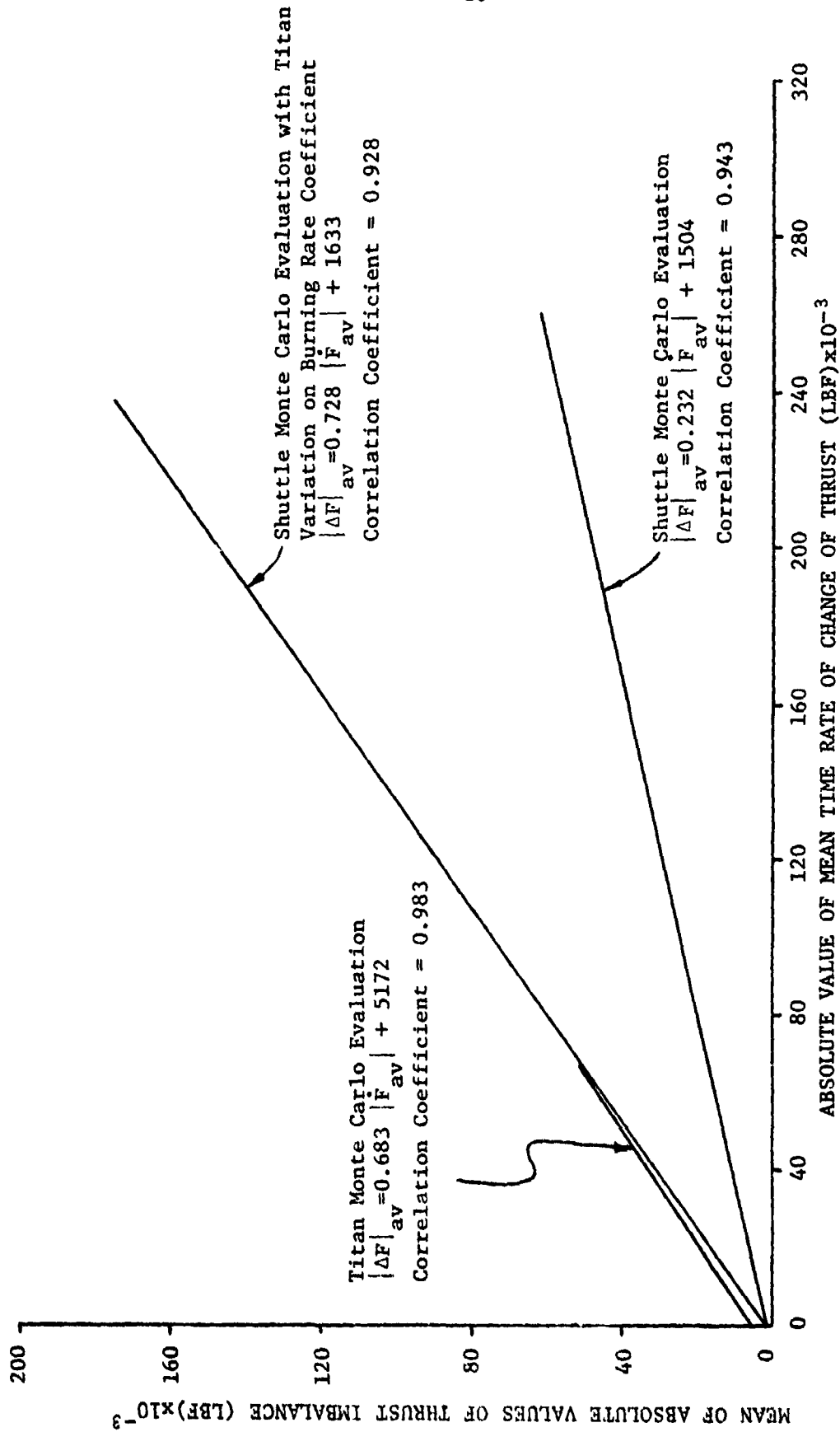


Figure II-4. Comparison of Space Shuttle and Titan IIIC Monte Carlo evaluations demonstrating the effect on thrust imbalance correlations of variations of burning rate coefficient.

where CV_N is the coefficient of variation of the burning rate coefficient for the new motors and τ_N (in inches) is the mean web thickness of the new motors. This relationship is obtained by assuming linear relationships between the product of CV and τ and the slope and intercept of the thrust imbalance versus thrust-time slope.

The discussion to this point has dealt only with thrust imbalance correlations; however, an identical procedure has been executed simultaneously to establish correlations for the standard deviation of the thrust imbalance. Fig. II-1b represents the standard deviation correlation for the Titan theoretical pairs; Fig. II-2b for the Space Shuttle theoretical pairs; and Fig. II-3b for the Space Shuttle theoretical pairs using Titan variations and web adjustment on burning rate coefficient. These analyses are compared in Fig. II-5 to illustrate the effect of the burning rate adjustment on the standard deviation. Since the comparison is similar to that demonstrated in Fig. II-4 for the thrust imbalance, a relationship for the standard deviation of the thrust imbalance for a pair of new motors is determined,

$$s_{|\Delta F|} = (-0.00126 + 2.969 CV_N \tau_N) |\dot{F}_{av}| + (606 + 20,610 CV_N \tau_N), \quad (II-6)$$

again without the Monte Carlo evaluation.

Linear least squares approximations to the actual relationships between thrust imbalance, standard deviation and thrust-time slope have been established, but nothing has been said about the applicability of these correlations. We wish to use these approximations to establish an expected thrust imbalance envelope for the Space Shuttle theoretical SRM pairs, as was accomplished in Ref. 2, using the relationship

$$\Delta F = \pm K_2 [|\Delta F|_{av}^2 + s_{|\Delta F|}^2]^{1/2} \quad (II-7)$$

where K_2 is the two-sided tolerance factor (3.68) determined by the sample size (30 pairs) and the desired probability (0.90) that a specified percentage (99.7%) of the thrust imbalance distribution will be included within the prescribed limits (thrust imbalance envelope).

A comparison is presented in Fig. II-6 of the thrust imbalance envelopes using the Monte Carlo evaluations directly and using the linear approximations. For conciseness only the positive halves of the envelopes are presented; the negative halves are simply mirror images. Fig. II-6a demonstrates a close agreement of the two methods during the tailoff period. This is a result of the relatively close correlation of the linear approximation to the Monte Carlo data during tailoff, as seen in Fig. II-2. However, Fig. II-6b does not indicate a close agreement of the

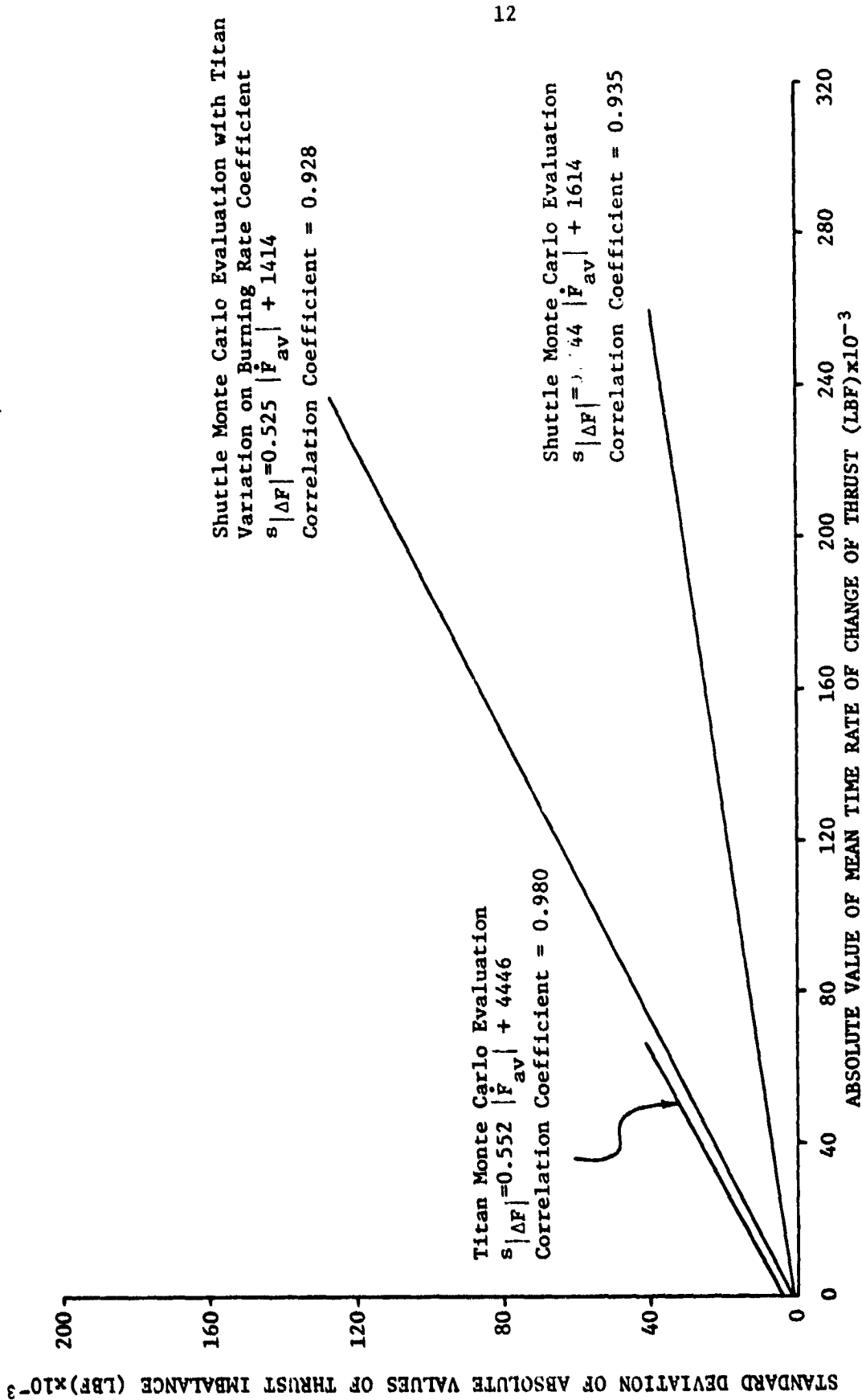
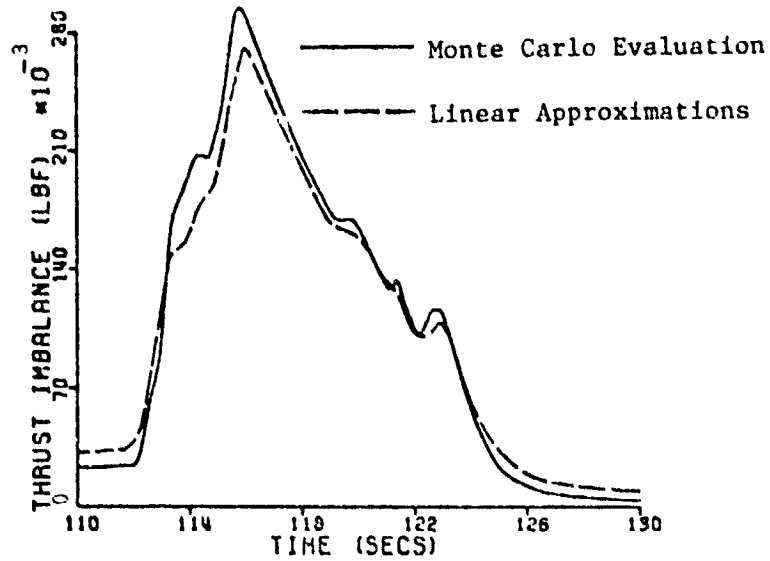
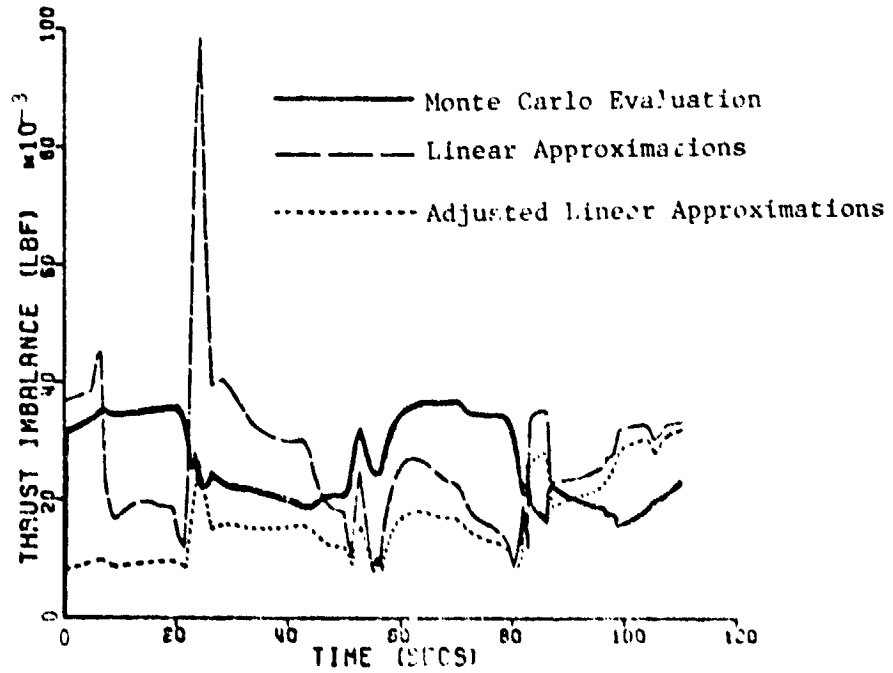


Figure II-5. Comparison of Space Shuttle and Titan IIIC Monte Carlo evaluations showing the effect of variations of burning rate coefficient on the thrust imbalance standard deviation correlations.



a. Thrust imbalance envelopes during tailoff.



b. Thrust imbalance envelopes during web action time.

Figure II-6. Tolerance limits for thrust imbalance of 30 theoretical Space Shuttle SRM pairs (Probability 0.90 for 99.7% of the distribution).

two methods during web action time, especially at the end of the head end star grain web action time. This discrepancy can be explained since the slopes of the linear approximations were determined principally by the tailoff characteristics, and the associated greater web action times tend to magnify any variations in burning rate at shorter times. Therefore, the slopes of the linear approximations are accurate only during the tailoff period. The slope can be adjusted by reducing it in proportion to the percentage of web burned at any particular time. Continuous adjustment of the slope throughout web action time results in the third thrust imbalance envelope represented in Fig. II-6b. This adjustment does result in much closer agreement at the end of star grain web action time, but adversely affects most of the remaining envelope. Since the linear approximations are reasonably accurate only for higher values of thrust-time slope, it can be argued that the web-time adjustment should only be applied to higher magnitudes, such as at the end of the star grain web action time. This would, however, present difficulties in transition between adjusted and non-adjusted portions of the envelope.

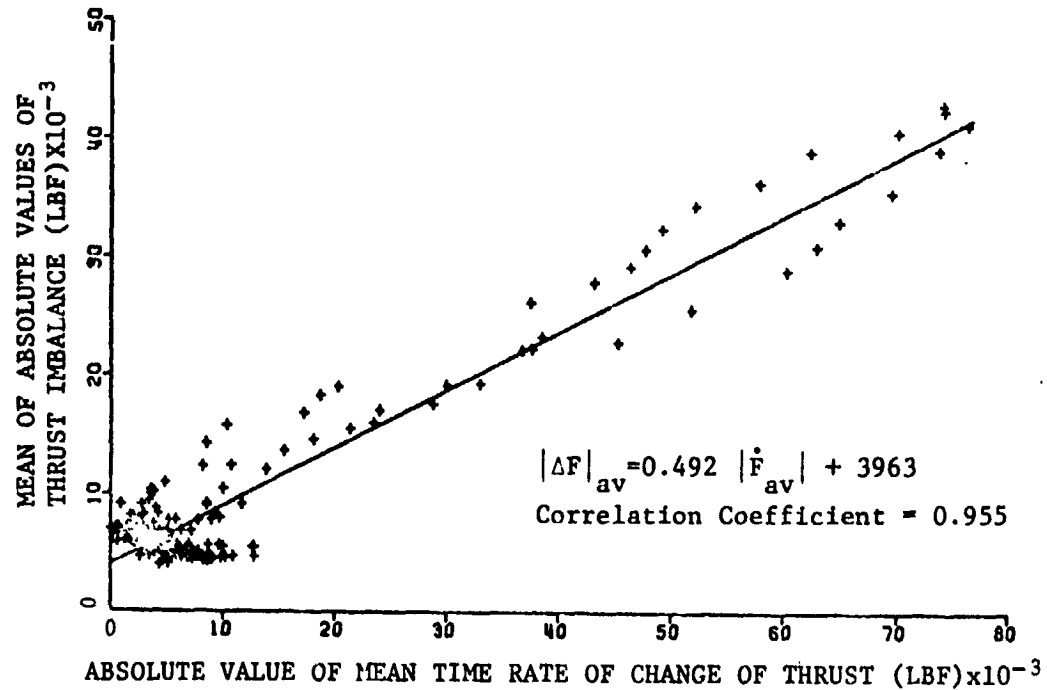
Since the linear approximations of the thrust imbalance and the standard deviation of the thrust imbalance are reasonably accurate only during tailoff, a better approximation of the tailoff imbalance envelope could possibly be achieved by using only the tailoff trace to determine the linear approximations.

Because of the somewhat random relationship between thrust imbalance and thrust-time slopes during web action time, this portion of the envelope should be used only as a first, and generally not conservative, estimate. For the tailoff period, an alternative method has been devised whereby the thrust imbalance characteristics obtainable from the Monte Carlo program can be estimated quite well from the nominal thrust-time trace using the linear approximation given by Eqs. II-5 and 6. The equations are only valid, however, for motors having manufacturing and processing variations similar to the Titan IIIC and Space Shuttle SRM's, except for burning rate control, which is accounted for in the equations.

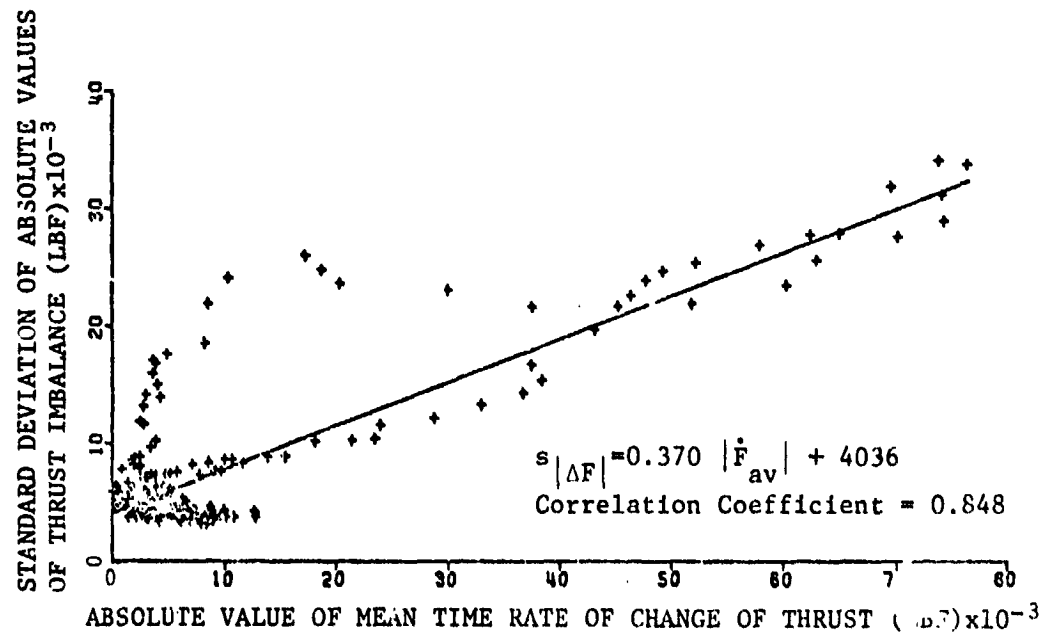
Comparison with Test Results

Thrust imbalance relationships have now been established between Monte Carlo evaluations of two different SRM configurations. The question now arises as to how these theoretical evaluations compare with actual test data. At present, the Space Shuttle SRMs have not flown and no test data for motor pairs is available, so we can institute a comparison only for the Titan IIIC configuration, for which good paired thrust data is readily available for 20 SRM pairs.

Thrust imbalance and thrust-time slope are correlated for the 20 Titan IIIC SRM pairs of test data in an identical manner as performed previously for the theoretical motor data. Figure II-7a depicts the



a. Thrust imbalance vs. thrust-time slope.



b. Standard deviation of thrust imbalance vs. thrust-time slope.

Figure II-7. Correlations determined from flight data obtained from a set of 20 Titan IIIC SRM pairs.

results of this correlation along with a linear least-squares approximation $|\Delta F|_{av} = 0.492 |\dot{F}_{av}| + 3963$, with a correlation coefficient of 0.955. Comparison of the flight data and theoretical motor correlations reveals significant differences in thrust imbalance characteristics. Because the equations used in the Monte Carlo evaluation do not represent all the complex phenomena associated with the beginning of tailoff, the resulting theoretical traces initially regress more abruptly than the actual performance traces. Therefore, the maximum thrust imbalance is higher and occurs earlier in the theoretical motor pairs than in the actual pairs which have more rounded traces at the beginning of tailoff. It is also notable that whereas the Monte Carlo program overestimates the maximum imbalance based on the present time slice analysis, it underestimates the maximum thrust imbalance calculated without regard to the time at which that maximum occurs (See Ref. 2).

Because of the nature of the differences in tailoff characteristics between the theoretical and actual Titan IIIC motors, it is reasonable to assume that these differences will be exhibited in other configurations such as the Space Shuttle SRMs. With this assumption it is now possible, using the theoretical Space Shuttle SRM thrust imbalance correlation (Fig. II-2a), to predict the thrust imbalance correlation of the flight article. Using the proportionate changes in slope and intercept between the Titan correlations (Figs. II-1 and 7) and applying these to the Space Shuttle theoretical correlation (Fig. II-2), results in the Space Shuttle flight prediction as depicted in Fig. II-8 which is $|\Delta F|_{av} = 0.167 |\dot{F}_{av}| + 1152$. Additionally, it may be noted that a proportionate increase in maximum thrust-time slope is included in the Space Shuttle prediction, since this increase is also exhibited by the Titan motors during tailoff. A similar scaling is applied to the standard deviation of the thrust imbalance as indicated in Figure II-9. The Space Shuttle flight prediction of the standard deviation is then $s_{|\Delta F|} = 0.097 |\dot{F}_{av}| + 1465$.

Using these flight predictions (scaled linear approximations), an expected tailoff thrust imbalance envelope is determined and presented in Fig. II-10a. The validity of the scaled thrust imbalance envelope can be verified by examination of the Titan IIIC theoretical and test data. Figure II-10b depicts the thrust imbalance envelope computed from: 1) the Monte Carlo Evaluation, directly; 2) linear approximations of the Monte Carlo evaluation; 3) scaled linear approximations (flight predictions); and 4) actual test data. It is noted that the scaled envelope is slightly lower than that of the test data. This is because the linear approximations of the test data (Fig. II-7) do not accurately represent the maximum values of thrust imbalance and standard deviation since these values lie off the regression line. Also, in Fig. II-10a, the time of peak thrust imbalance differs between the Monte Carlo and the test data analyses, as described previously in this report. However, the magnitude of the peak imbalance is fairly accurately represented by the flight prediction envelope.

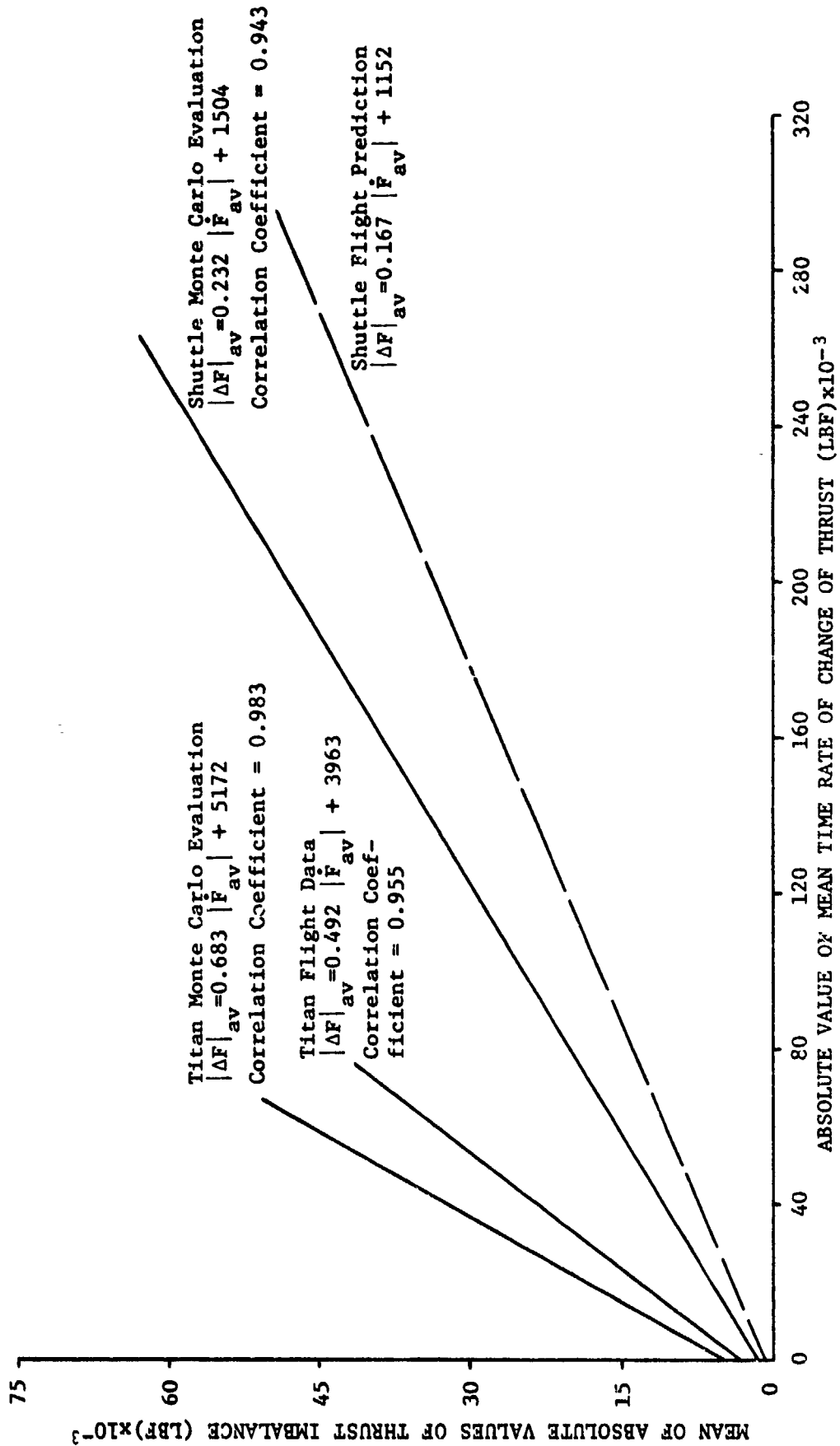


Figure II-8. Scaling of the Space Shuttle theoretical thrust imbalance correlation to establish the Space Shuttle flight prediction correlation.

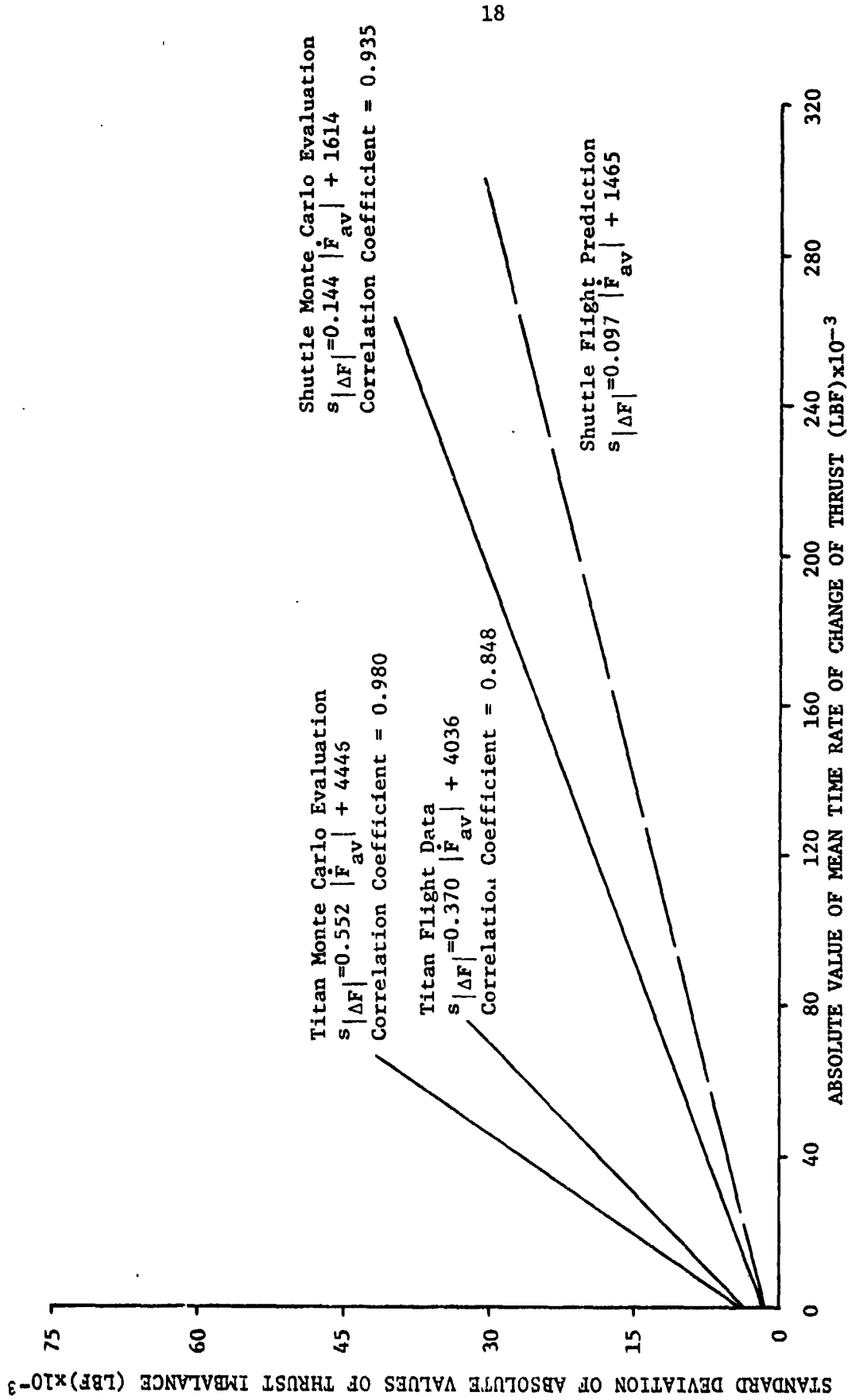
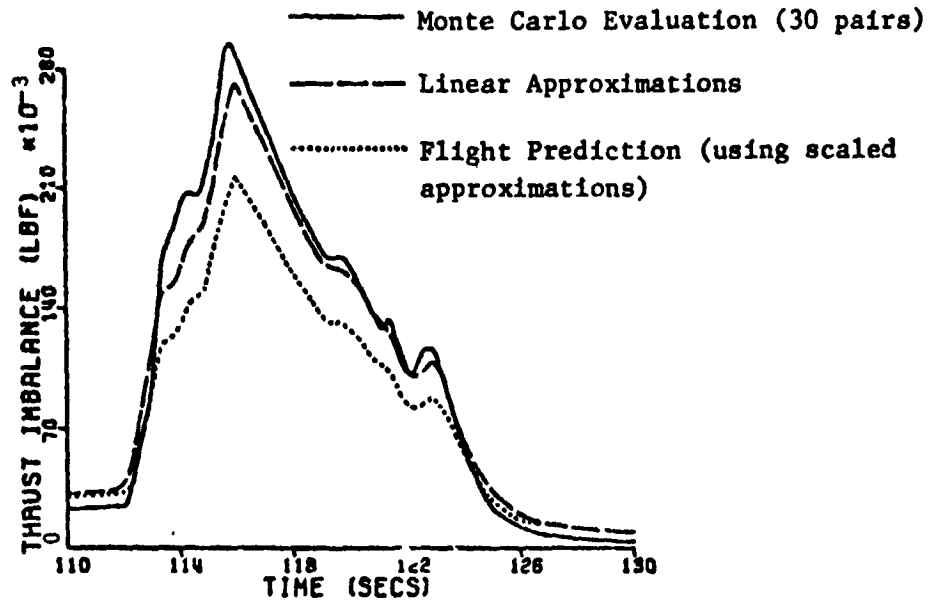
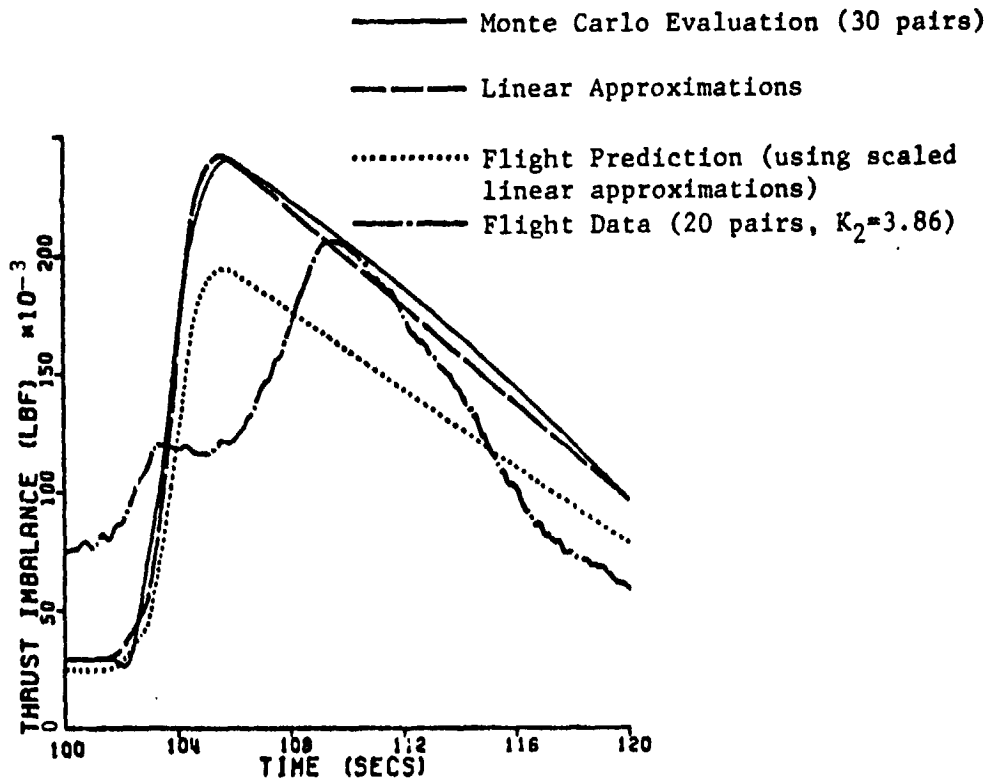


Figure II-9. Scaling of the Space Shuttle theoretical thrust imbalance standard deviation correlation to establish the Space Shuttle flight prediction correlation.



a. Space Shuttle thrust imbalance envelopes.



b. Titan IIIC thrust imbalance envelopes.

Figure II-10. Tailoff thrust imbalance tolerance limits (probability 0.90 for 99.7% of the distribution)

The scaling relationship between the theoretical evaluation and flight test results may be applied either to the new procedure with no Monte Carlo analysis or to a Monte Carlo analysis of a new SRM pair. The latter alternative is recommended when manufacturing and processing controls differ substantially from those employed in the Titan IIIC.

III. IMPROVEMENT OF PREVIOUS COMPUTER PROGRAMS

Because of the anticipated use of the design analysis and Monte Carlo computer programs in the preliminary design of SRMs, it is desirable at this time to increase the efficiency of the programs and reduce some of the complexities associated with handling of data. This is accomplished through an extensive series of modifications aimed at reducing computer execution time, reducing program size, eliminating unnecessary variables, statements and computations, reducing the amount and number of cards of input data, allowing more flexibility and easier modification of input data, and reducing the volume of output data.

Design Analysis Computer Program

In an attempt to accomplish the aforementioned goals, many modifications have been made. The following represents a list of the most significant modifications since Ref. 3:

1. The data card to 'SET INITIAL VALUES OF SELECTED VARIABLES TO ZERO' is removed and this operation replaced by utilizing available temporary disk space.
2. All input data except NRUNS and tabular data for propellant temperature distribution are converted to NAMELIST inputs. This facilitates easier data input since specific format fields are not required. Variable names must be punched on the cards, thus allowing more rapid identification of variables and their values. The use of NAMELIST eliminates repetitious input of data when running multiple configurations since only the variables with different values from the first case need to be input. Note that this is slightly different from the normal NAMELIST feature of updating the previous case. This is done using temporary disk storage. Three NAMELIST blocks are used:

MAIN1 includes all variables previously read in data groups in the MAIN program, except for NRUNS and the tabular input of the propellant temperature distribution (ITEMP = 0).

AREAS1 includes all variables previously read in data groups in subroutine AREAS, except for the tabular input of burning areas.

AREAS2 includes all the variables for the tabular input of burning areas (INPUT = 1 or INPUT = 3).

An example of the use of these NAMELIST blocks in multiple configurations is given in Table III-1. For multiple cases, blocks MAIN1 and AREAS1 must be included in all cases even if no variables are listed (See AREAS1 block of second case in Table III-1). NAMELIST is a standard FORTRAN IV feature, and additional information can be obtained from any good reference in FORTRAN IV.

3. The use of NAMELIST now allows the elimination of the input variable NTABY, which was necessary to insure the reading of all tabular input data cards before proceeding to the next data case. When data is read from NAMELIST, preceding unread data cards are skipped, thus eliminating the previous need to do this using NTABY.
4. The input variable MU is eliminated since it is only used for calculating the initial Reynolds number, which is not used elsewhere. Obviously the calculation and output of initial Reynolds number are also eliminated.
5. An output option (IOO) is included in NAMELIST MAIN1 to allow a reduction in output volume.

The options for IOO are:

0 for partial output (2 lines)

1 for full output (4 lines)

Tables III-2 and III-3 illustrate partial and full outputs, respectively, and include various other input options.

6. An input variable (PATMI) for the initial atmospheric pressure (in psia) is included in NAMELIST MAIN1 to accommodate pressures other than standard (14.696 psia).
7. Numerous repetitious computations are consolidated, and some program logic is optimized. This does much to reduce the required execution time of each configuration.
8. The convergence criteria (GMAX and GMIN) on the chamber pressure iterations are slightly relaxed. This gives a reduction in execution time, while not adversely affecting the program results.
9. In the output data, FAV and FVACAV have been replaced by AVRAD and AVEPS, which are the average nozzle throat radial erosion rate (in in/sec) and the average nozzle expansion ratio, respectively.

Table III-1. Sample input of multiple configurations for the design analysis computer program.

```

NUM9FR OF CONFIGURATIONS TO BE TESTED = 16*0
EMAINI IGO=0, IWO=0, ICC=0, IPO=0, NUMPLT=16*0
NTAB=0, RN2NI=46667, RHO=0, A1=.006915, ALPHA=0.0, BETA=1.0,
, ITEMP=1,
CSTAR=5162.1, NI=0.750, L=1381.31, TAU=42.32, DE=145.64, DTI=54.43, THETA=0.0,
ALFAN=12.31, LTAP=244.25, XT=10.4, ZO=3.27, CSTART=3.8E-5, PTRAN=70.0,
DELTA=0.04, XOUT=1000.0, DPOUT=1000.0, ZETA=0.9617, TB=123.4, HB=140463.0,
GAME=1.141, ERRFF=0.0, XOUT=1000.0, DPREF=832.0, DTREF=54.584, PIPK=0.0015, TREF=60.0,
GAREAS1 INPUT=3, GRAIN=3, STAR=2, NT=0, ORDER=1, COP=1, DO=144.58, DI=59.67,
NS=0.0, LGS1=177.28, NP=11.0, RC=71.41, LGNI=56.6, THETCN=0.0, THETCH=90.0,
GAREAS2 YT=4.00, ABPK=-18810.0, ABSK=0.0, ABNK=0.0, APNK=0.0, APNK=0.0, VCIT=0.0,
GAREAS2 YT=9.50, ABPK=-9370.0, ABPK=-9370.0, ABPK=-9370.0, ABPK=-9370.0,
GAREAS2 YT=20.20, ABPK=14290.0, ABPK=14290.0, ABPK=14290.0, ABPK=14290.0,
GAREAS2 YT=24.00, ABPK=-34400.0, ABPK=-34400.0, ABPK=-34400.0, ABPK=-34400.0,
GAREAS2 YT=41.49, ABPK=-19520.0, ABPK=-19520.0, ABPK=-19520.0, ABPK=-19520.0,
GAREAS2 YT=42.85, ABPK=-41000.0, ABPK=-41000.0, ABPK=-41000.0, ABPK=-41000.0,
GAREAS2 YT=50.00, IGO=1, IWO=1, IPO=3, NUMPLT=0.0, IGO=1, IWO=1, IPO=3, NUMPLT=0.0,
IGO=1, IWO=1, IPO=3, NUMPLT=0.0, IGO=1, IWO=1, IPO=3, NUMPLT=0.0, IGO=1, IWO=1, IPO=3, NUMPLT=0.0,
RIG=1720.0, DELTIG=0.005, PBIG=700.0, CSIG=4900.0, PMIG=1600.0, TIL=.1, T12=1.5,
DTFMP=30.0, SIGMAP=.03, SIGMAS=.02, X1=3.0, X2=0.0, SYNCNOM=1.9E5, DCC=155.5,
PSIC=1.4, DELC=.283, LCC=1102.5, NSEG=5.0, HCN=62.0, SYNNO=1.9E5,
PSTS=1.4, PSIA=2.0, KI=.208, K2=.0925, PSTINS=2.0, DELINS=.0462,
KEH=.003, KEN=.012, DLINER=.033, TAU=.065, WA=0.0,
TTAB=85.0
TTAB=73.0
TTAB=74.0
END
GAREAS1 YT=0.0, ABPK=-19110.0, ABPK=-19110.0, ABPK=-19110.0, ABPK=-19110.0,
GAREAS2 YT=2.00, ABPK=-15840.0, ABPK=-15840.0, ABPK=-15840.0, ABPK=-15840.0,
GAREAS2 YT=8.80, ABPK=20510.0, ABPK=20510.0, ABPK=20510.0, ABPK=20510.0,
GAREAS2 YT=23.91, ABPK=-12910.0, ABPK=-12910.0, ABPK=-12910.0, ABPK=-12910.0,
GAREAS2 YT=40.89, ABPK=-33260.0, ABPK=-33260.0, ABPK=-33260.0, ABPK=-33260.0,
GAREAS2 YT=41.77, ABPK=-5770.0, ABPK=-5770.0, ABPK=-5770.0, ABPK=-5770.0,
GAREAS2 YT=43.01, ABPK=-10540.0, ABPK=-10540.0, ABPK=-10540.0, ABPK=-10540.0,
GAREAS2 YT=43.40, ABPK=-41000.0, ABPK=-41000.0, ABPK=-41000.0, ABPK=-41000.0,

```

Table III-2. Sample of partial output (I00=0) from the design analysis computer program.

```

*****
**** EQUILIBRIUM BURNING ****
*****
I= 0.3      RHOZ= 3.9004E-01  PHEAD= 8.215E 02  MDOZ= 1.1210E 04  MNOZ= 2.4754E-01
Y= 0.3      SUMAB= 4.450E 03  SG= 1.15849E 03  DT= 5.442499E 01  FVAC= 2.970E 06  P= 2.7121960E 06

TABULAR VALUES FOR YI= 4.000  READ IN
APNK= 0.0  APHK= 0.0  APNK= 0.0
I= 0.121    RHOZ= 3.8951E-01  PHEAD= 4.026E-01  PUNOZ= 7.701E 02  MDOZ= 1.1162E 04  MNOZ= 2.4712E-01
Y= 0.043    SUMAB= 4.453E 03  SG= 1.158476E 03  DT= 5.443179E 01  FVAC= 2.978E 03  P= 2.6986620E 06

I= 0.202    RHOZ= 3.8948E-01  PHEAD= 4.025E-01  PUNOZ= 7.698E 02  MDOZ= 1.1158E 04  MNOZ= 2.4668E-01
Y= 0.080    SUMAB= 4.457E 03  SG= 1.158461E 03  DT= 5.443358E 01  FVAC= 2.9734E 06  P= 2.6885520E 06

*****
**** TAIL OFF BEGINS ****
*****
I= 110.201  RHOZ= 3.2539E-01  PHEAD= 3.264E-01  PUNOZ= 4.469E 02  MDOZ= 6.8894E 03  MNOZ= 9.0267E-02
Y= 40.837  SUMAB= 3.281E 05  SG= 0.0  DT= 5.613434E 01  FVAC= 1.8069E 06  P= 1.8045730E 06

TABULAR VALUES FOR YI= 41.490  READ IN
ABNK= 0.0  APNK= 0.0
I= 110.323  RHOZ= 3.2531E-01  PHEAD= 3.253E-01  PUNOZ= 4.447E 02  MDOZ= 6.8557E 03  MNOZ= 9.0267E-02
Y= 40.477  SUMAB= 3.271E 05  SG= 0.0  DT= 5.613574E 01  FVAC= 1.7981E 06  P= 1.7957530E 06

*****
**** BEGIN HALF SECOND TRACE ****
*****
I= 166.694  RHOZ= 1.5525E-03  PHEAD= 1.552E-03  PUNOZ= 1.352E-01  MDOZ= 2.0890E 00  MNOZ= 9.0267E-02
Y= 43.477  SUMAB= 2.182E 04  SG= 0.0  DT= 5.619614E 01  FVAC= 5.4779E 02  P= 5.4656958E 02

I= 134.232  RHOZ= 0.0  PHEAD= 0.0  PUNOZ= 2.943E-06  MDOZ= 2.943E-06  MNOZ= 9.0267E-02
Y= 43.517  SUMAB= 1.676E 04  SG= 0.0  DT= 5.619644E 01  FVAC= 0.0  P= 0.0

```

OVERALL *QTR CHARACTERISTICS

```

YPI= 1.1032E 06
MP2= 1.1029E 06
AP= 1.1033E 06
PHMAX= 8.4326E 02
ISPVAC= 2.5190E 02 02
ITDI= 2.6310E 08
ITVAC= 2.7793E 08
AVRAD= 4.9029E 08
AVEPS= 6.8148E-03
PMWAV= 6.2028E 00
VCI= 4.0051E 02
VCF= 4.2809E 06
LAMBDA= 2.1660E 07
LAMBDA= 8.0237E-01

```

ORIGINAL PAGE IN
OF POOR QUALITY

10. The special relationship used to calculate head end chamber pressure for combination circular-perforated and star grains is eliminated. The same approximate relationship is now used for all grains, because detailed examination of results over a period of several years shows the special relationship tends in general to underestimate the head end pressure.

These modifications have resulted in substantial savings in both the number of input data cards (approximately halved) and execution time of the design analysis program. With a full output (I00 = 1, Table III-3) the reduction in execution time is approximately 20 percent, and more significantly, with a partial output (I00 = 0, Table III-2) the reduction in execution time is approximately 40 percent, and the volume of output is approximately halved. This reduction in execution time should, however, not be misinterpreted as a reduction in total computer time or compilation time. While the compilation time comprises, by far, the majority of the total computer time for a single run, and has not been reduced by this effort, the compilation time can be totally avoided by the use of an object deck, i.e., a copy of the program which has already been converted to machine language and requires no compilation time. Thus the reduction in execution time is most significant when using an object deck or when running multiple configurations.

The entirety of these modifications have also been applied to the design analysis program with grain deformation (Section IV) along with additional modifications unique to the grain deformation analysis and the addition of a new erosive burning law options. These additional modifications are discussed in Section IV.

Monte Carlo Computer Program

Since the Monte Carlo Program is composed, in part, of the design analysis program, most of the modifications described above can be utilized. Modifications number 1, 6, 7, 9, and 10 are applied to the Monte Carlo program. Modification number 2 is also adopted insofar as the non-statistical input variables are concerned. The modifications described in number 7 are extended to include that portion of the program unique to the Monte Carlo program. In addition to these modifications, the input option IRAND is eliminated so that only the random number generator RANDU is used. The GAUSS (machine independent) random number generator is eliminated as an option since the true randomness of this generator as adapted into the Monte Carlo program is questionable. An example of the Monte Carlo input data is illustrated in Table III-4. Note that a change in the statistical input data format is incorporated, in conjunction with the NAMELIST modifications, to reduce the total number of input data cards by approximately one-half. An example of the Monte Carlo program output is shown in Table III-5.

As in the design analysis program, a considerable savings in execution time is realized in the Monte Carlo program using these modifications.

ORIGINAL PAGE IS
OF POOR QUALITY

29

In order to assess the reduction in execution time, a sample set of 60 motors (30 SRM pairs) is analyzed. The reduction in execution time is approximately 20 percent. Unlike the design analysis program, the execution time of the Monte Carlo Program represents, by far, the majority of the total computer time, resulting in a considerable savings even though no significant reduction in compilation time has been achieved.

IV. EFFECTS OF GRAIN DEFORMATION ON INTERNAL BALLISTICS

Reference 2 explains how deformation of the propellant grain can affect the propellant burning rate and account for a significant portion of the "scale factor" between large motors and small ballistic test motors. The important factor is the tangential strain at the burning surface of the propellant grain. A method developed by Smith (Ref. 9) was used in Ref. 2 to estimate the strains at various times for circular-perforated grains. The method was coupled with the design analysis computer program to analyze the effects on internal ballistics. Comparisons were presented of internal ballistic test data and theoretical evaluations with and without grain deformation for the Titan III C/D and Castor TX354-5 SRMs. Although good results were obtained with the grain deformation analysis, it was felt that additional verification of the method was needed before the analysis is incorporated into the Monte Carlo computer program. Also, the effects of star-type grain deformation needed to be investigated.

It was planned to test the hypothesis on circular-perforated grain deformation on two additional SRMs: the TU-455.02 (64 in. dia.) and the Space Shuttle nozzle erosion test motor. However, the erosion test motor proved inappropriate because the grain was not case-bonded. Also, the anomalous performance of the TU-455.02 indicated that additional factors were involved which affected the burning rate (Ref. 10). The irregular behavior of this SRM thus masked our early efforts to ascertain the effects of grain deformation. This led first to investigation of potential effects of nozzle throat variations during SRM operation and finally to a semi-empirical analysis of propellant erosive burning characteristics. Details of these analyses are presented in this Section along with comparisons of test data for the TU-455.02, Castor TX354-5 and the first Space Shuttle SRM (DM-1) with theoretical results using the grain deformation analysis and a new burning rate model. Also presented is an investigation of the effects of star-type grain deformation. This includes both an experimental test using an inert subscale model of the Space Shuttle star grain segment and a theoretical finite element analysis.

Investigation of Nozzle Throat Variation

Several large SRMs including the previously mentioned TU-455.02 were shown by Ref. 10 to have actual pressure-time curves which did not match theoretical predictions. These motors were found to have a consistent pattern of deviation. The pattern was such that the actual pressure was lower than theoretical over the first and last portion of the trace and higher than theoretical during intermediate portions. The deviation was explained in terms of a burn-rate variation with web thickness. A term known as the burn-rate anomaly rate factor (BARF) was defined as the ratio of actual burn-rate to theoretical burn-rate. Reference 10 discussed

some of the possible causes of the BARF variation but did not present any theory to completely explain the phenomenon. Some of the possible causes mentioned were grain design, deformation of grain, temperature gradient, and propellant characteristics.

The design analysis program with grain and case deformation effects was used during the present study to verify that deformation could not by itself account for BARF variations. Indeed, in the case of TU-455.02, the deformation effect seems to increase the initial BARF. The negative result raises the question of whether burn-rate is the parameter that varies with time or whether other parameters cause the burning rate anomaly.

Nozzle throat variations during motor operation is next examined to determine if the deviation in chamber pressure could be caused by a nozzle throat area deviation. The scheme used to deduce nozzle throat diameter, in the absence of direct measurement, is to compare the experimental thrust and head end pressure for a particular SRM to obtain the apparent throat diameter. This gives throat diameter as a function of time. The nozzle diameter can thus be found, independent of any burn-rate effects.

The first step in this iterative procedure is to assume a nozzle throat area. Next, the Mach number at the nozzle end of the port is determined from the ratio of the area of the port to the area of the throat, using the isentropic relation,

$$M = (A^*/A) \{ 2[1+(\gamma-1)M^2/2]/(\gamma+1) \}^{(\gamma+1)/2(\gamma-1)} \quad (IV-1)$$

The nozzle end stagnation pressure P_{on} is found from the experimental head end pressure P'_h from the following equation which can be obtained from relationships given in Ref. 11,

$$P_{on}/P'_h = [1+(\gamma-1)M_n^2/2]^{\gamma/(\gamma-1)} / (1+\gamma M_n^2) \quad (IV-2)$$

Eq. IV-2 is based upon a constant port area. Applied to a quasi-steady state situation, it is independent of the burning rate distribution over the propellant surface.

The exit Mach number is determined from the nozzle expansion ratio using Eq. IV-1. The exit pressure is obtained from the exit Mach number and the stagnation pressure. Assuming isentropic flow in the nozzle,

$$P_{on}/P_e = [1+(\gamma-1)M_e^2/2]^{\gamma/(\gamma-1)} \quad (IV-3)$$

The ideal thrust coefficient is then computed from

$$C_{F_o} = \left\{ \left[\frac{2\gamma^2}{\gamma-1} \right] \left[\frac{2}{\gamma+1} \right]^{(\gamma+1)/(\gamma-1)} \left[1 - \left(P_e / P_{on} \right)^{(\gamma-1)/\gamma} \right] \right\}^{1/2} \quad (IV-4)$$

The thrust is obtained from

$$F = \zeta_F \left[P_{on} A^* C_{F_o} + A_e (P_e - P_a) \right] \quad (IV-5)$$

and is compared with the experimental thrust F' . If the difference between computed and experimental thrust is greater than a specified tolerance, a new A^* is computed from

$$A^* = \left[F' / \zeta_F - A_e (P_e - P_a) \right] / (P_{on} C_{F_o}) \quad (IV-6)$$

and the iteration continues with a new evaluation of M_n ; otherwise the time and port radius is incremented and the next experimental values used.

The SRMs investigated using this procedure are the TU455.02, the LPC-156 Jet Tab, the AGC-260-1, the AGC-260-2, the TCC 156-2C-1 and the TX354-5 of References 12 through 17, respectively.

The variation in nozzle throat diameter with time for each of these motors is given in Fig. IV-1. A linear interpolation between the actual initial and final throat diameter is also shown on the figure. Some error in the results can be attributed to the necessity of obtaining data from plots in test reports. Also, for several of the SRMs which were fired vertically, it was necessary in the test reports to add the total weight of propellant burned at each time to the corresponding thrust. Inaccuracy in estimating the burned mass can also contribute some error to the results. However, the motors generally show an initial apparent closing down of the throat possibly due to mass blocking effects from low available energy propellant gases emanating from the aft end of the grain. The analysis does not provide a scheme to account for such two-dimensional nozzle flow phenomena. An additional source of error in the analysis is that some of the SRMs have a slight axial taper to their ports while Eq. IV-2 is based on constant port area. However, burning rate is used in the analysis only for evaluation of the port diameter as a function of time, and errors from this source should be small at least for the initial portion of the trace where there appears to be some effect of nozzle throat variation not accounted for in the usual nozzle erosion models. Beyond this, the results are inconclusive and do not by themselves explain the burning rate anomaly.

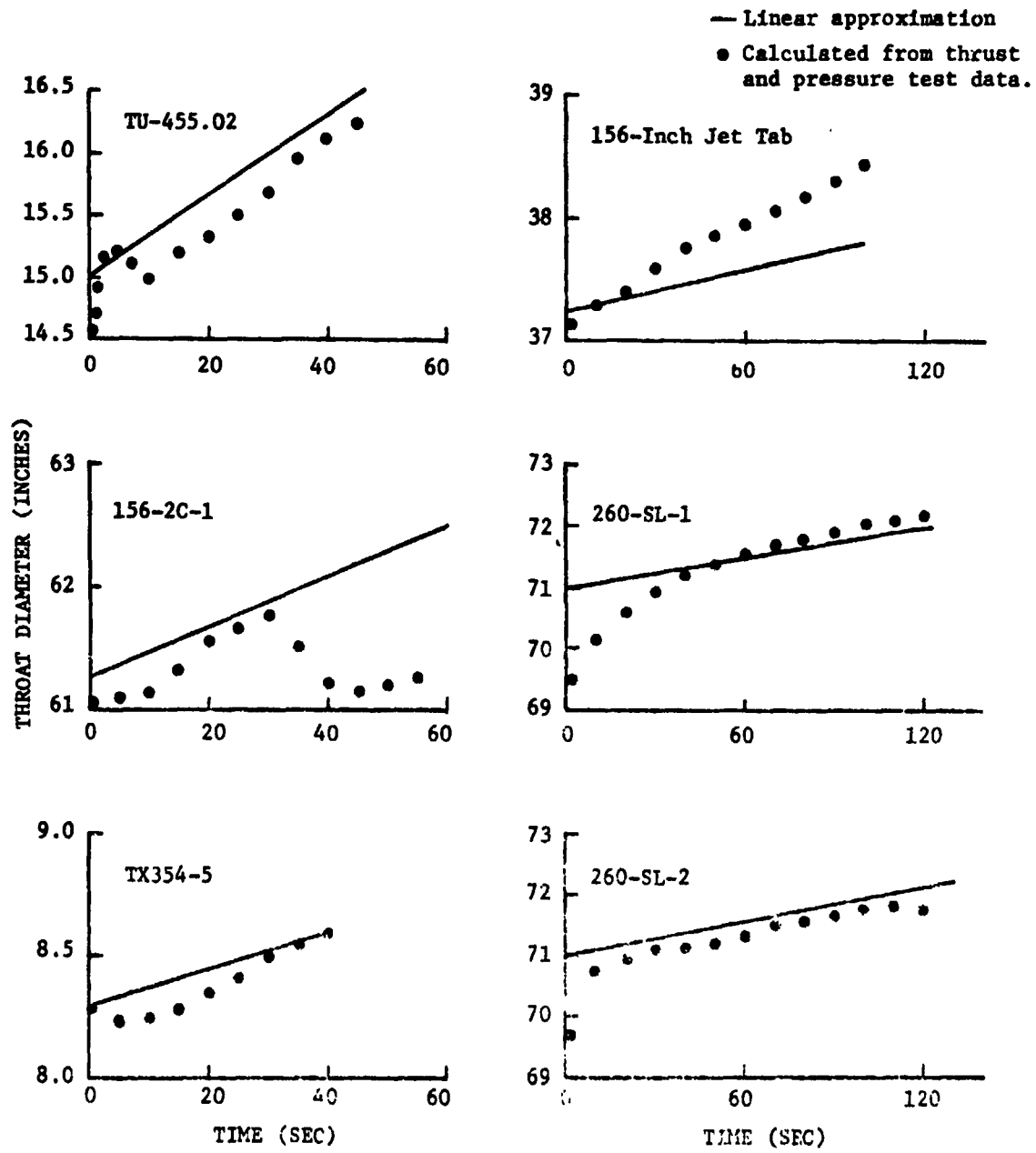


Figure IV-1. Variation in nozzle throat diameter with time.

Burning Rate Model

Since the nozzle throat area investigation failed to give a clear explanation of the burning rate characteristics of the SRMs examined, attention was directed to other possible causes of the anomalous behavior. The TU-455.02 was selected for the initial investigation because the BARF effect was so pronounced in this SRM. Although Ref. 10 examines a variety of potential causes of the burning rate anomaly, no investigation of the contribution of erosive burning is discussed in the reference. This is possibly because measured chamber pressures are generally lower than predicted for the initial portions of the pressure-time traces in the TU-455.02 and other SRMs examined in Ref. 10, and this is the reverse of what one would expect from erosive burning. However, we observed that the measured chamber pressures are initially low in the motors exhibiting BARF and it is well known that erosive burning rates are quite sensitive to pressure (Ref. 18). This led to an investigation of erosive burning as a possible cause of the burning rate anomaly.

The first effort was strictly empirical and was directed toward determining a coefficient, $a(u)$, and an exponent, $n(u)$, in the relationship

$$r = a(u) r^{n(u)} \quad (IV-7)$$

that gives a good match between test data and theoretical performance. The design analysis computer program was used to obtain the predicted performance.

The design analysis program calculates two burning rates: one near the nozzle end of the propellant grain at the point of maximum Mach number and one at the head end where $u=0$. To obtain the total mass flow rate upstream of the point of maximum Mach number a linear average of the two burning rates is taken (Ref. 5). While introducing some question as to the accuracy of the resultant calculations, the use of this simplified program permits economical assessment of SRM performance (Over 100 separate performance predictions were made in the investigations discussed in this subsection). The appropriateness of linear averaging of burning rates is discussed further later in the report and a modification to the method introduced. In calculating the head end burning rate, the a and n corresponding to small ballistic test motor rates, assumed to give zero velocity behavior, were used wherever possible for each SRM examined in the course of this study so as not to confound the investigation with artificial "scale factors." For the TU-455.02, it was necessary to estimate the zero velocity rate from performance of the large motor somewhat prior to tailoff since the ballistic test motor rate was unavailable. Grain deformation was not accounted for in the first evaluation.

After a large number of runs with the design analysis program wherein various simple functions of u for a and n at the nozzle end of the grain

were tested, a fair match was obtained. The results were not improved in general by consideration of grain deformation. Similar empirical expressions failed badly when tested for Castor TX354-5. The investigation did reveal that there is an apparent general depression of the burning rate coefficient and increase in burning rate exponent in Eq. IV-7 at the higher flow velocities which is not inconsistent with the qualitative erosive burning behavior of many propellants. In particular it has been demonstrated (Ref. 18) that some propellants exhibit a threshold velocity below which the burning rate is lower than for zero velocity. The threshold is in general lower for higher pressures and one might alternatively speak of a threshold pressure below which velocity depresses burning rate. The threshold velocity (or pressure) is not usually very high but it should be kept in mind that even for an SRM with small port-to-throat area ratio a substantial portion of the propellant surface is subjected to low velocities even during the initial portion of SRM operation. Thus it seems that the low velocity regime is worthy of additional investigation. Several of the more widely used erosive burning rate laws do not even permit representation of burning rate depression, notable among which is the law of Robillard and Lenoir (Ref. 18).

Since a relationship of the form of Eq. IV-7 having general applicability was not found, the investigation turned to an examination of alternative relationships. Poor results have been obtained in previous investigations with the design analysis program using the law of Robillard and Lenoir (Ref. 5). This law uses an approach which is more or less conventional in its treatment of the erosive burning effect as one that is strictly additive to the rate obtained at zero velocity. In the present investigation, we take the alternative approach of considering the erosive effect to be one of direct reduction of the flame height and, following Summerfield (Ref. 18, p. 38) on ammonium perchlorate composite propellants, take the burning rate to be inversely proportional to the average flame height.

The usual form of the Summerfield formula applicable in the absence of erosive burning is

$$1/r_0 = c_1/P + c_2/P^{1/3} \quad (\text{IV-8})$$

The formula fits experimental burning rate data about as well as $r_0 = ap^n$ (Ref. 18, p. 38). The first term on the right-hand side of Eq. IV-8 represents the contribution of the diffusion flamelets to the average flame height while the second term gives the effect of the surface covering by premixed flames. In the presence of erosive burning, Barrère and Larue and others treat the constant c_2 as a function of velocity and the exponent of P in the last term of Eq. IV-8 is assigned a value of $2/3$ (Ref. 18, p. 436 and p. 445). Our results with attempts to match test performance of TU-455.02 with similar representations are unsatisfactory.

We next hypothesize that a reduction in flame height and a corresponding inversely proportional increase in burning rate accompanies the establishment of a flow velocity over the surface of the propellant and the effect on flame height is subtractive so that

$$1/r = 1/r_0 - c_3 \text{Re}^{0.5} (1 - P_{cr}/P) / L \quad (\text{IV-9})$$

Here $r_0 = aP^n$ is used to represent the burning rate in the absence of velocity rather than the more complicated relationship, Eq. IV-8, as a matter of convenience. The form for the last term in Eq. IV-9 evolved after a number of comparisons with the test performance of both TU-455.02 and Castor TX354-5. In Eq. IV-9, Re is the flow Reynolds number and it was found during the comparisons that best results are obtained with a Reynolds number based on flow-path length. Also, it was observed that the ratio of the pressure above a certain critical pressure P_{cr} to the pressure P itself plays an apparently important role in the reduction of flame height over and above that played by Re, hence the term $(1 - P_{cr}/P)$. The investigation was conducted to obtain the best matches between theoretical and test performance without grain deformation being taken into account. About equal quality results are also obtained for the two SRMs with an exponent on Re of 0.8. However, when grain deformation effects are included, the exponent of 0.5 proves better. Higher powers of $(1 - P_{cr}/P)$ were also considered but give poor results.

The viscosities of the propellants in this study are considered to be substantially the same so that the final form of the equation used to calculate the burning rate at the point of maximum flow Mach number is:

$$1/r = 1/r_0 - c_4 (GL_{ref}/L)^{0.5} (1 - P_{cr}/P) \quad (\text{IV-10})$$

Here L_{ref} is the initial "controlling" grain length of the TU-455.02 (205.75 in.) which is used as a reference dimension in the development and G is the mass flow rate per unit area at the point of maximum Mach number.

Although results with the modified flame height law (Eq. IV-10) combined with the grain deformation are quite good for the TU-455.02 and TX354-5, for both SRMs, the theoretical analysis yields pressure-time traces that rise progressively, somewhat above the actual performance traces, as tailoff is approached. One explanation is that Eq. IV-10, while containing a threshold pressure, does not represent the velocity sensitivity of this threshold; that is, the threshold pressure is the same at all velocities, so that as long as $P > P_{cr}$, the erosive rate is greater than the zero velocity rate no matter how low the flow velocity. This discrepancy is adjusted to some extent in the new analysis by modifying the distribution of

burning rate over the grain. In place of using a linear average of head and nozzle end rates to calculate the mass generated, the average burning ratio is taken as

$$r_{av} = 0.5[1+(y/b)^5]r_h + 0.5 [1-(y/b)^5]r_n \quad (IV-11)$$

where b represents the average web thickness of the main propellant grain:

$$\begin{aligned} b &= r_w - |z/2| - x_{Ta} \quad (y < b) \\ b &= y \quad (y > b) \end{aligned} \quad (IV-12)$$

These relationships cause the average burning rate to rapidly approach the zero velocity rate in practical SRMs as tailoff is approached while having negligible influence during about the first two-thirds of web action time. Although strictly empirical, the approach seems reasonable for at least partially compensating for the fact that the linear average clearly becomes inadequate as burning progresses and more and more of the burning surface is subjected to less than threshold velocities.

Final Comparisons with Test Data

The final comparisons with test data are presented in Figs. IV-2 and IV-3 for the TU-455.02 and TX354-5, respectively. Results are given based on the modified flame height model both with and without grain deformation being taken into account. Values of the constant material parameters used are identified on the figures. It is notable that the best fits are obtained for both SRMs when the grain deformation effect is included in the evaluations.

As a final test, an evaluation was performed for the Space Shuttle SRM and comparison made with the test data from the first development motor (DM-1) using the "as built" configuration. The Space Shuttle SRM has a PBAN type propellant quite similar to that of the TU-455.02 except that a different curing agent and a somewhat different percentage of burning rate catalyst is used. For the Space Shuttle evaluation, the TU-455.02 constants were used in the flame height law. For the Space Shuttle deformation analysis, the reported Poisson's ratio of 0.499 was used while for the TU-455.02, the reported ratio of 0.4995 was used. The results are shown in Fig. IV-4. In this case, a better match is obtained without the grain deformation. However, the analysis with grain deformation would be as good or better if a Poisson's ratio of 0.4995 were used in the Space Shuttle evaluation and would be definitely better than the corresponding analysis without deformation if the erosion constants were adjusted for the best fit with grain deformation using the reported values of Poisson's ratio.

We feel that the results of this study provide additional support for the validity of the grain deformation analysis as well as a new approach

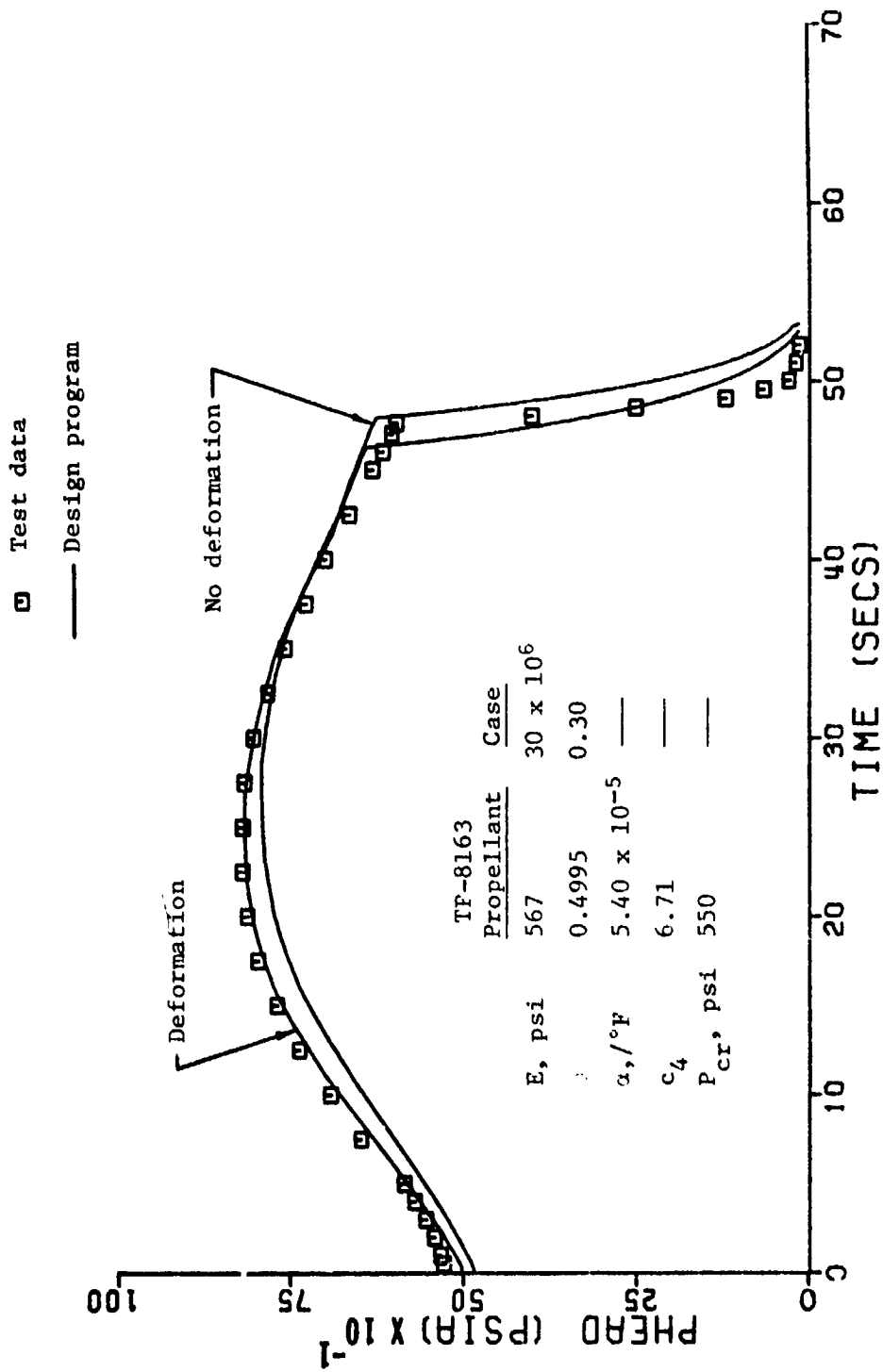


Figure IV-2. Comparison of test data for the TU-455.02 SRM with theoretical performance calculated using the modified flame height burning rate model.

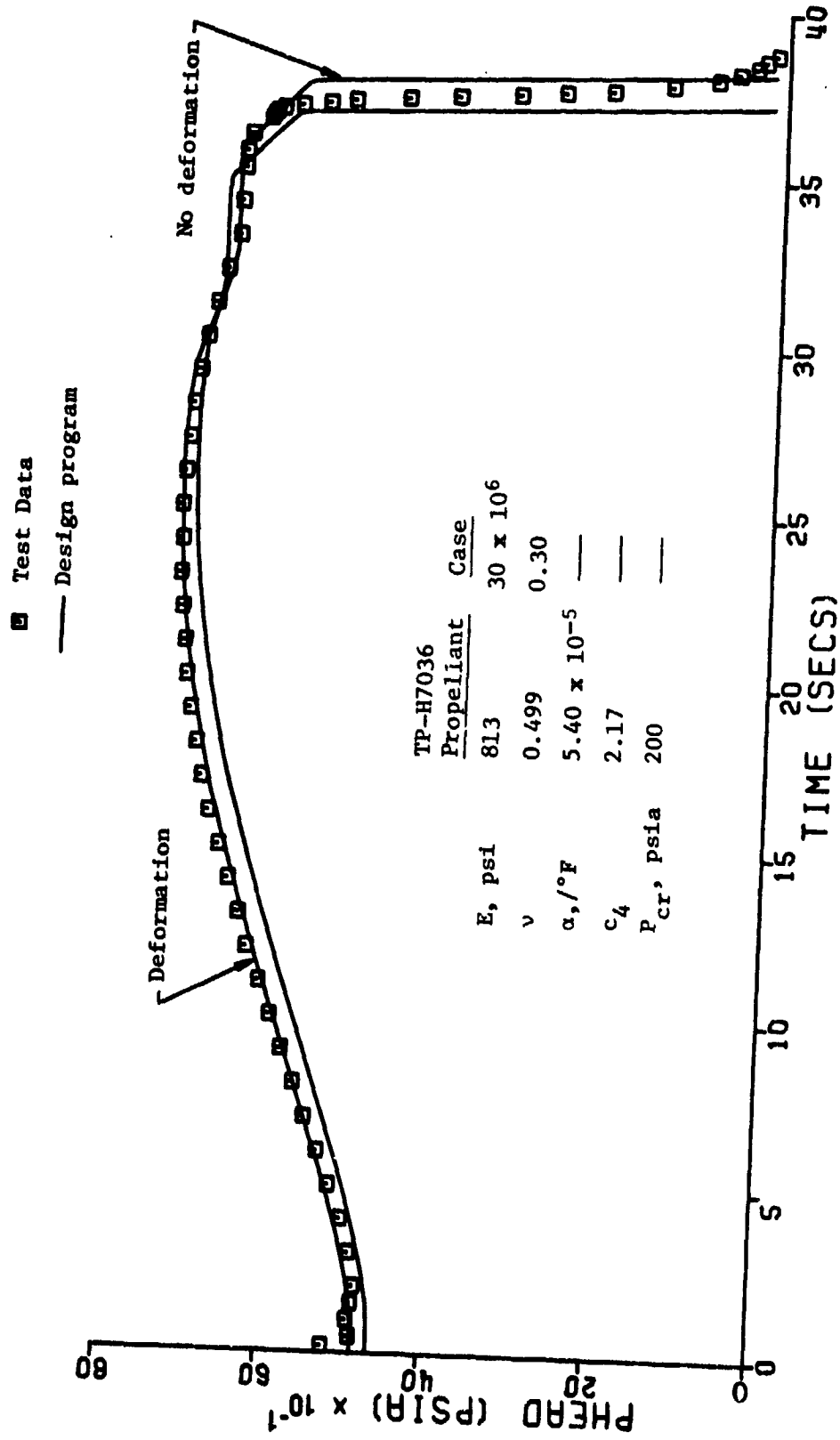


Figure IV-3. Comparison of test data for the TX 354-5 SRM with theoretical performance calculated using the modified flame height burning rate model.

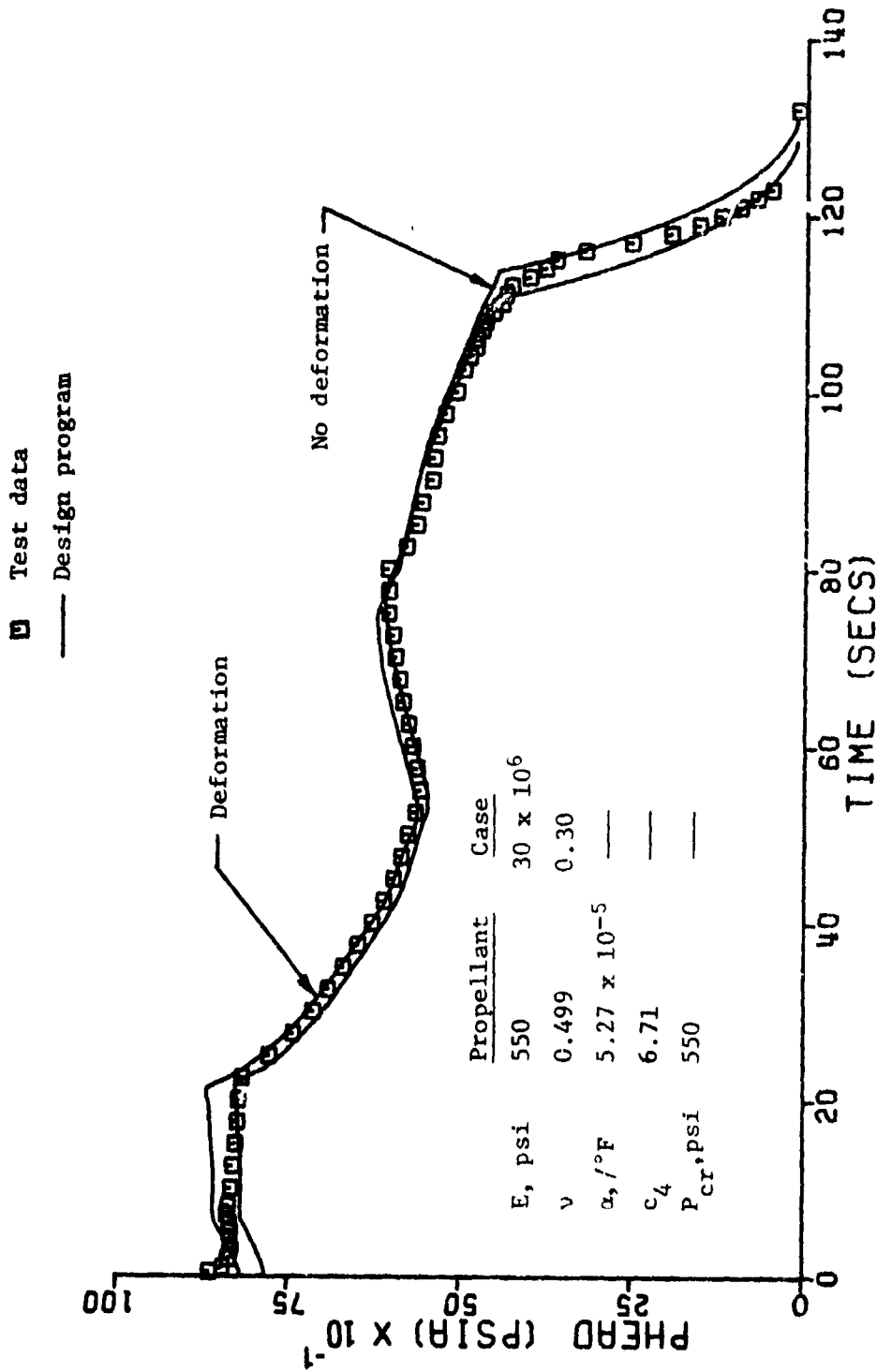


Figure IV-4. Comparison of test data for the Space Shuttle SRM (DM-1) with theoretical performance calculated using the modified flame height burning rate model.

to representation of erosive burning phenomena that is worthy of further examination. However, the results for the Space Shuttle SRM introduced some questions about the applicability of the grain deformation that should be resolved before this approach is incorporated into the Monte Carlo program. Also, the burning rate model should be tested in a more comprehensive analysis which computes local burning rates at a large number of stations throughout the propellant length while providing for threshold velocities in a more realistic manner than the simplified design analysis program. Improvement of the basic burning rate law expression is clearly possible. For example, a brief investigation has shown that the law as presently formulated does not fit the performance of small ballistic test motors but that better results are probably obtainable with larger exponents on the Reynolds number term.

It also may be possible to find a better approach than that provided by Eqs. IV-11 and IV-12 to account for threshold velocity in the simplified design analysis program. The fact that, for each of the three SRMs examined, the predicted traces still tend to rise above those of the measured data as talloff is approached is quite possibly due to inadequacy of the design analysis program in its artificial treatment of the threshold velocity effects.

Further study of the effects of nozzle throat area variations may provide a means of improving prediction of chamber pressures for the initial portion of the trace where, for the three cases presented, the predicted pressures are low. This phenomenon as previously noted might well be due to mass blocking of the throat by low available energy flow from the aft end of the propellant. Simple representation of this blockage may be possible within the framework of the design analysis program, and, of course, would be applicable to more sophisticated programs employing the modified flame height model.

Deformation of Star Grains

A portion of the Space Shuttle SRM head end segment contains a star-type grain. In the grain deformation analysis using the modified design analysis program, deformation of star grains is disregarded. We next examine the validity of this assumption making use of both experiment and theory with particular emphasis on the Space Shuttle SRM.

For the experimental investigation, a scaled model of the cross-section of the forward segment of the Space Shuttle's Solid Rocket Motor was constructed. An aluminum mold was constructed with dimensions that were 1/36 of those of the actual Shuttle motor.

The material selected to represent the grain was Dow Corning's 3110 RTV silicone rubber. This material consists of a white liquid encapsulant and a

curing agent. The cured material has mechanical properties approximately equivalent to those of the Space Shuttle propellant. Using a mixing ratio of 1 part curing agent to 10 parts of encapsulant, the mixture was prepared and poured into the aluminum mold. The silicone rubber was allowed to cure for 48 hours. The model was then separated from the mold and the excess material was trimmed off. The thickness (length) of the finished model was 1/2 in. and the diameter 4 in.

A three-piece chamber was constructed from a 1/2-inch thick sheet of Plexiglas (See Fig. IV-5). The center portion of this chamber consisted of a Plexiglas ring to which the silicone model was glued to represent case-bonding. The ring was then sandwiched between two Plexiglas discs and the three pieces were bolted together with sixteen bolts. Clearance space was provided on both sides of the model and the Plexiglas discs. A pressure tap was inserted through the center of one disc. A steel cylindrical container filled with mineral oil was connected by hoses to the Plexiglas chamber. A steel plunger was inserted into the top of the cylindrical container so that a load could be applied to the plunger and model by a universal tension-compression testing machine. A Bourdon-tube pressure gage was connected to the hose between the cylinder and the piston (top photograph, Fig. IV-5). An extensometer was mounted as shown in the bottom photograph on Fig. IV-5 for the purpose of recording changes in diameter of the chamber.

A five-inch rectangular bar was poured from the same mixture that was used to cast the model. After curing, this bar was inserted into the universal testing machine. At various loads, the length and width of the bar were measured. From a plot of the stress-strain curve determined from the elongation of the bar as a function of applied load, the value of Young's modulus was found to be 500 psi. By plotting the change in width against the change in length at each load, the value of Poisson's ratio was determined from the slope of the resulting curve to be 0.498.

A camera with a close-up lens was placed in front of the assembled chamber and model. The camera was focused so that one star point completely filled the frame. A picture was taken at 0 psi (gage pressure). Using the universal testing machine, a load was slowly applied. A picture was taken at each 50 psi increment up to and including 400 psi. The photographs were developed as 8 x 10 enlargements. By tracing the perimeter of the star point at 0 psi and 400 psi, the change in perimeter could be calculated. Also, by superimposing these two traces as in Fig. IV-6, the deflection of the star point could be observed. Figure IV-6 shows the deflection of the star point at 400 psi as compared to its initial position at 0 psi. The point was found to elongate slightly in the radial direction and contract in the circumferential direction. The perimeter was found to increase by 0.22% at 400 psi.

A theoretical investigation of the deformation of star grains due to pressurization was also performed using a finite element computer program. The purpose of this investigation was to determine the magnitude of deforma-

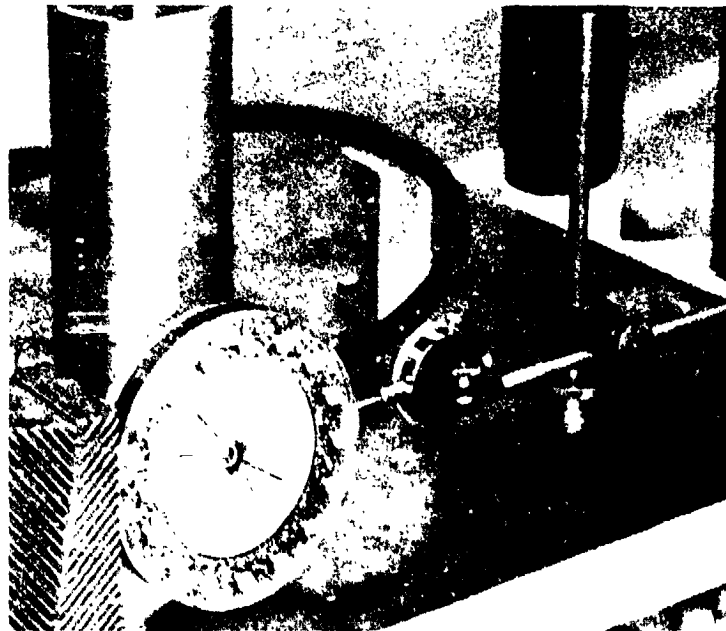
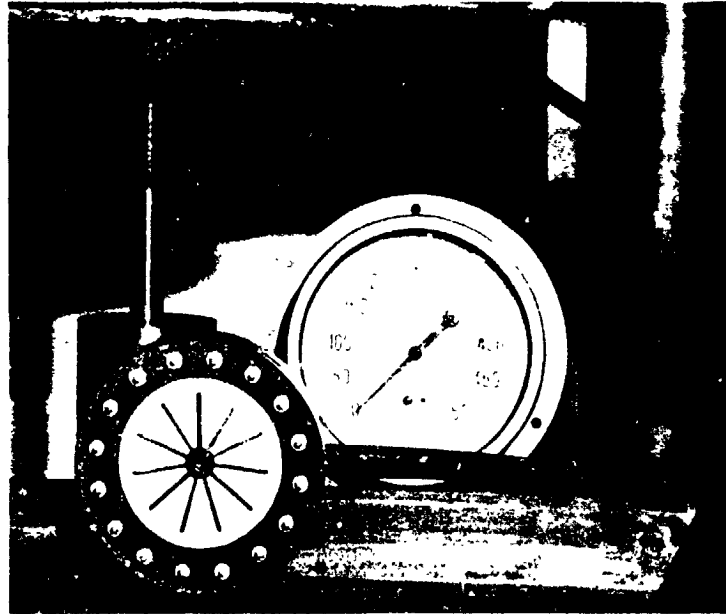


Figure IV-5. Test setup for determination of star grain perimeter changes under pressurization.

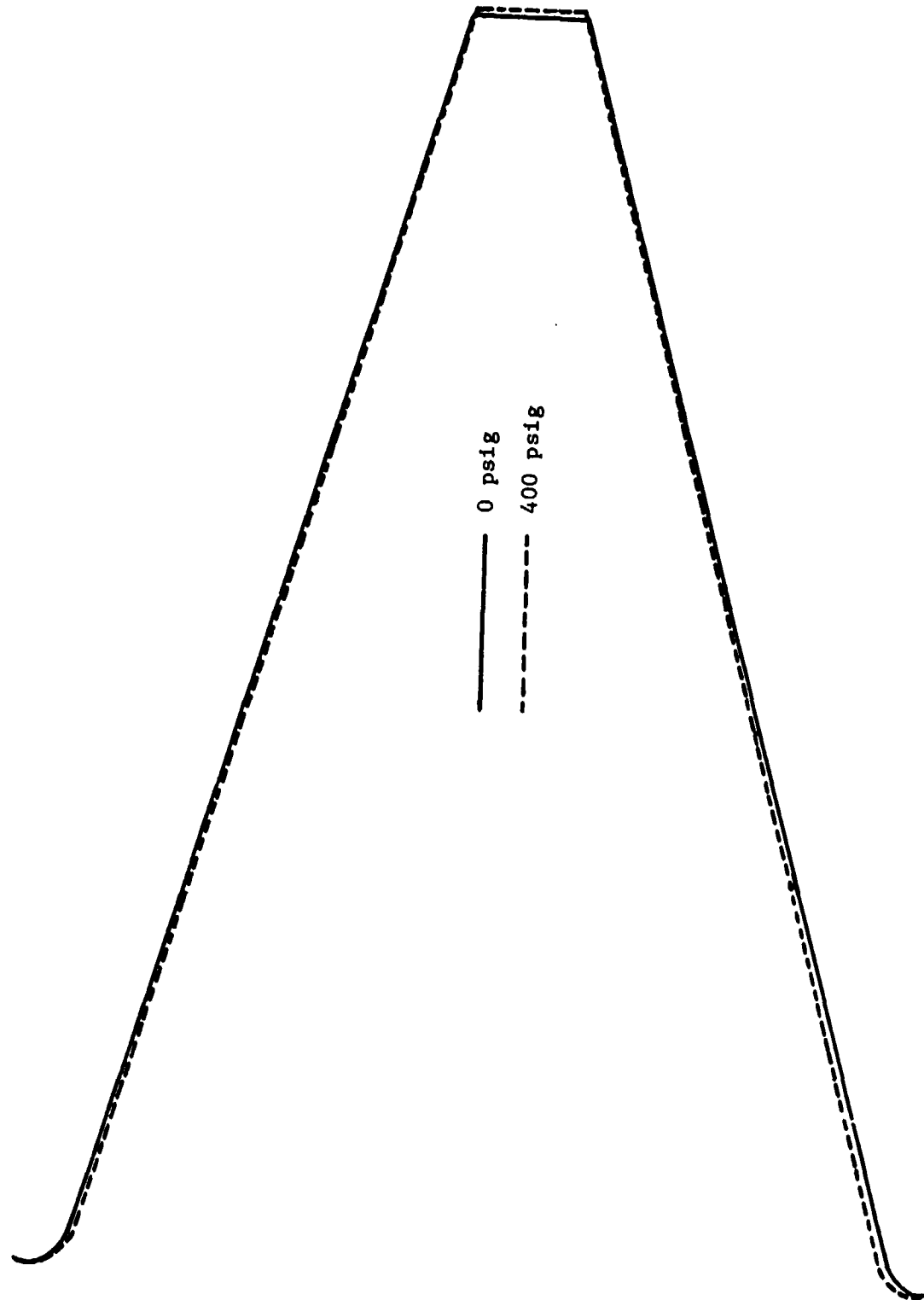


Figure IV-6. Superimposed tracings of enlarged photographs of subscale Space Shuttle star point model under 0 and 400 psig pressurization.

tion, correlate the results with experimental data and, if necessary, apply proper adjustments to the design analysis program, preferably with a simple approach.

The computer program used in this analysis was obtained from Ref. 20 and was modified for use on the IBM 370/158. The program performs a two-dimensional stress-strain analysis of a propellant grain, for a condition of either plane strain or plane stress. A condition of plane strain was used for this investigation since as shown in Ref. 9 when the grain is case-bonded longitudinal strains are small.

The accuracy of the program was tested using a finite element model of a circular-perforated grain. Results of this test indicated that deformations computed by the program were consistent with those computed with the equations of Refs. 2 and 9. A major subprogram was added to the finite element program for automatic grid generation of finite element models of standard and truncated star grains using inputs identical to the design analysis program. Another subprogram was coded for computing the change in perimeter of standard and truncated star grains due to deformation.

The Space Shuttle SRM star grain initial geometry was input to the finite element program with a chamber pressure of 300 psig. The computed change in perimeter was -5.3 in. or a decrease of 0.46%. This amounts to a total change in burning area of -939.6 in.² for the star grain or a decrease of 0.21% in total burning area including the circular-perforated grain area. A finite element model corresponding to the subscale experimental model was also input to the program with a pressure of 400 psig. The case modulus value was adjusted to obtain theoretical case deformations equivalent to the measured case deformation. This resulted in a decrease in perimeter of 0.3% as opposed to the increase of 0.22% measured in the experiment.

For this particular grain configuration the controlling parameter for the sign of the perimeter change is the length of the star point as compared with the web thickness and the width of the star point. Although the experiment was designed to approximate a condition of plane strain on the model, end effects may explain the differences. For the experimental model, 400 psi pressure was presumably applied to the end faces of the model, whereas, the finite element plane strain solution yielded axial stresses on the ends which were 0 to 40 psi less depending on the radial position. The lower end pressures would clearly cause the star points to be shorter and could account for the decrease in perimeter in the theoretical solution. Also, the finite element solution makes use of elements with straight sides producing some inaccuracies which can be minimized by increasing the number of elements. However, for the particular configuration tested, regardless of the sign, the magnitude of area change is small with respect to that produced by the circular-perforated grain deformation.

For other configurations of greater web thicknesses and shorter star points, the effects may be more significant. In general, the finite element

program could be used to relate pressure and star grain configuration parameters to change in perimeter. However, an overall program for internal ballistic analysis would be somewhat cumbersome since the perimeter changes would have to be evaluated at each increment of time. We feel that at least for star grains similar to those of the Space Shuttle, the effect of star grain deformation is insufficient to warrant the application of such a program. The studies thus far completed could prove of considerable value in finding a simplified approach to analysis of star grain deformation effects that would be consistent with the economy objective of the design analysis program.

Modification of the Deformation-Design Analysis Computer Program

All modifications to the design analysis program of Section III have been incorporated into the grain deformation design analysis program of Ref. 2. The purpose of these modifications as mentioned in Section III is to reduce computer execution time, program size, and input and output complexity. The equations for the modified burning rate model discussed in the present section have also been incorporated into the design analysis program as an option.

The basic inputs to the design analysis program with c.p. grain deformation and modified burning rate model options are identical to those for the design analysis program of Section III. Also required as inputs unique to the new program are the following variables specified in NAMELIST MAIN1:

1. Deformation inputs (Do not use if GRAIN = 2)

ISO = 0 for no deformation effects

 = 1 for deformation effects

PMOD = elastic modulus of the propellant, psi

CMOD = elastic modulus of the motor case, psi

PMU = Poisson's ratio for the propellant

CMU = Poisson's ratio for the motor case

ALPTS = Linear coefficient of thermal expansion of the propellant,
in/in

TAUC = Motor case thickness, inches

2. Modified burning rate model inputs

IRO = 0 for aP^n burning rate law

- 1 for Robillard-Lenoir erosive burning law

- 2 for modified flame height model (Do not use if IGO = 1)

ERCON = Coefficient of the erosive burning term for the modified flame height model, $(\text{sec}^3/\text{slug})^{1/2}$

PCRIT = Critical pressure in the modified flame height model, psia

LREF = Reference length in the modified flame height model, inches

It is not necessary to include these new variables when the effects are not desired; that is, when IRO or ISO is zero. Sample inputs and outputs for the grain deformation design analysis program with the modified burning rate law options are illustrated in Table IV-1 and IV-2, respectively.

V. THERMOMECHANICAL ANALYSIS

In Ref. 2, the variation in propellant burning rate due to thermoelastic coupling was shown to be a function of both elastic modulus and pressurization rate. Effects of the thermoelastic coupling on propellant burning rate was shown to be small in Ref. 2. However, the propellant modulus was chosen constant and as such was independent of spatial variations in temperature and strain rate. Both temperature and strain rate are known to have significant influence on the propellant modulus. Hence, it was decided to improve the propellant modulus model to account for spatial variations in temperature and strain rate before making a decision on the influence of the thermoelastic coupling.

In Ref. 2 an exponential pressure rise was used for the mechanical load. Under certain operating conditions the propellant may be subjected to an oscillating pressure load. The inherent irreversibility of the thermal processes produced by thermoelastic coupling makes this cyclic loading condition a likely candidate for producing changes in propellant temperature and hence in propellant burning rate. This loading condition is investigated in the present work using the improved model for the propellant modulus. The effects on thermoelastic coupling of varying Poisson's ratio, thermal conductivity and coefficient of expansion are also investigated in the present work.

A brief analysis of the effects of mechanical vibration on motor performance, including energy dissipation associated with viscoelastic materials is presented. Also discussed are the results of an internal ballistic analysis of ignition transients incorporating the Zeldovich and Novozhilov (Z-N) transient burning rate model (Refs. 2 and 7).

Propellant Modulus Model

The strain rate and temperature dependency of the modulus were modeled using the relaxation modulus model of Blatz (Ref. 21) shown in Eq. V-1.

$$E_R = (E_g - E_e) / [1 + t/t_0]^{10} + E_e \quad (V-1)$$

and the well known time-temperature shift factor of Williams, Landel and Ferry (Ref. 22) given by

$$\log_{10} a_T = C_1 (T - T_g) / (C_2 + T - T_g) \quad (V-2)$$

where the time, t , is given by $t = \Delta t/a_T$ and Δt is the time step used in the numerical solution of the thermoelastic problem.

The constants β_0 and τ_0 in Eq. V-1 and the constants C_1 , C_2 and T_g , the glass transition temperature in Eq. V-2, were obtained from Ref. 23 for Thiokol propellant TP-H8156. The constants E_e , the steady state or long time modulus, and E_g , the modulus at the temperature T_g , were adjusted to obtain a value of approximately 550 psi at 70°F. This was done because the constant propellant modulus used in the baseline analysis of Ref. 2 was 550 psi at 70°F.

The values used for the constants in Eqs. V-1 and V-2 are given in Table V-1.

Table V-1

Propellant Modulus Constants

β_0	0.164
τ_0	2.89×10^{-6} sec.
E_e	100 psi
E_g	31,250 psi
C_1	-17.44
C_2	51.6°K
T_g	243.15°K

A plot of the modulus versus temperature is shown in Fig. V-1.

The model described above was incorporated into the existing thermoelastic analysis computer program. An exponentially increasing pressure load, identical to that used in Ref. 2 was used with the new propellant modulus model. The results obtained are shown in Fig. V-2 compared to the baseline model in Ref. 2. In Fig. V-2, the ratio of the dynamic burning rate, r , obtained using the relaxation modulus and the Z-N model of Refs. 2 and 7 to the "steady state" burning rate, r_{ss} , obtained from

$$r_{ss} = aP^n \quad (V-3)$$

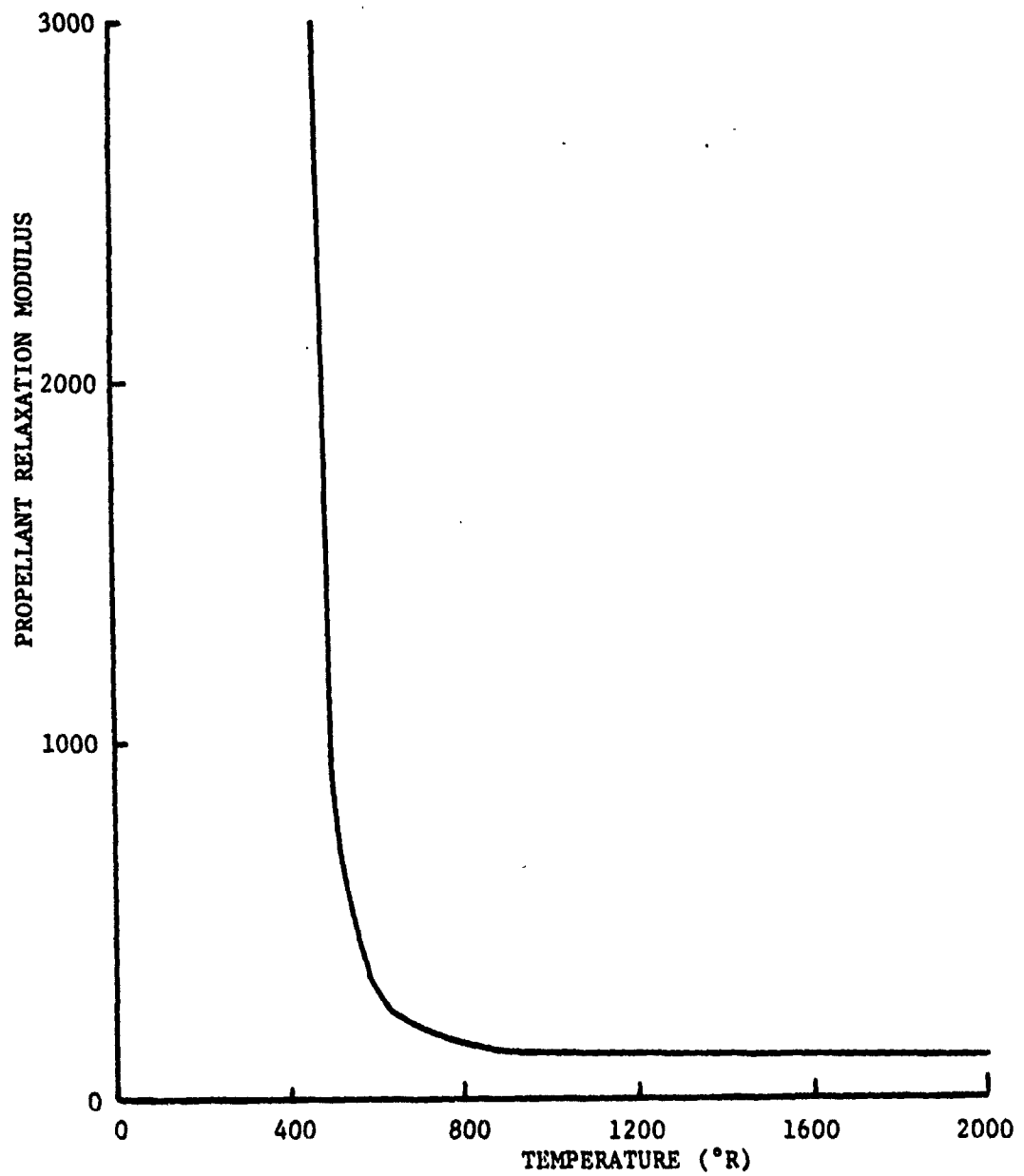


Figure V-1. Relaxation modulus versus temperature.

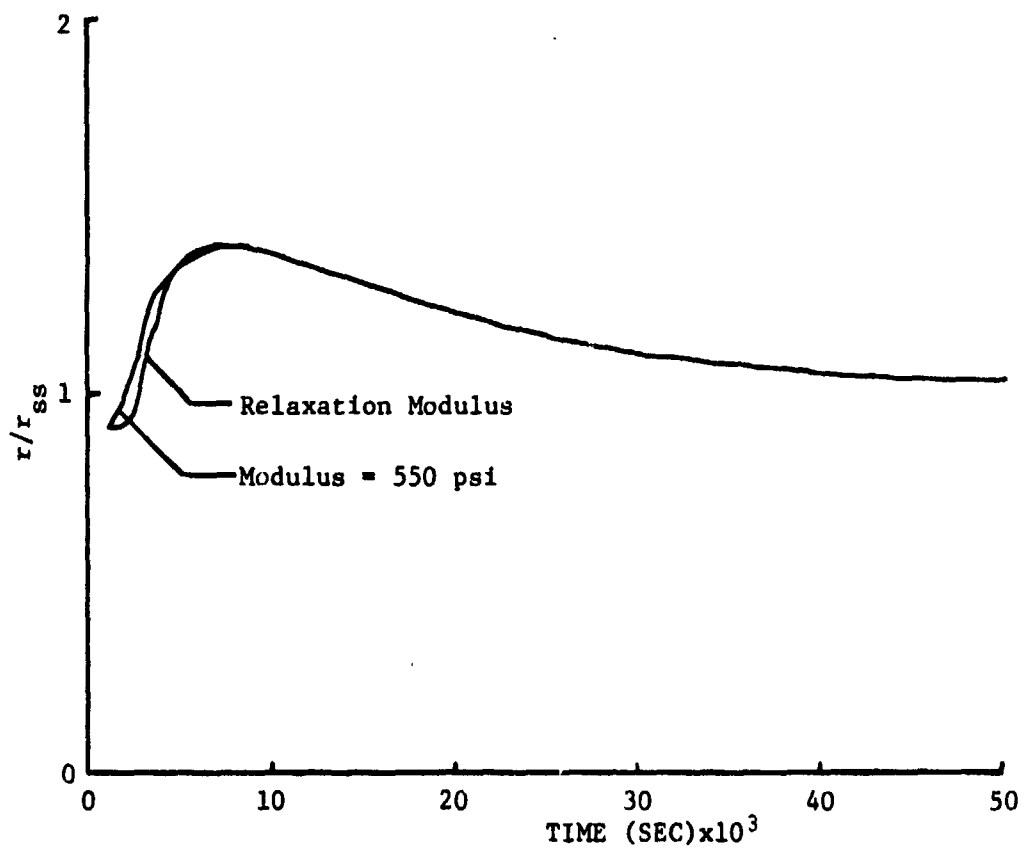


Figure V-2. Comparison of burning rate ratio for the constant propellant modulus model and relaxation modulus model.

is plotted versus time. The results using the new modulus model show essentially no difference between the two models except during the initial portion of the curve where there is less influence of thermoelastic coupling than was obtained previously. This is due to the lower value of propellant modulus at the higher temperatures near the burning surface. These results indicate that effects of thermoelastic coupling are probably negligible under the conditions anticipated in a Space Shuttle type SRM.

Figure V-3 shows the effect on propellant burning rate caused by changing the initial pressurization rate from 14000 to 28000 psi/sec. The relaxation modulus was used for both cases shown and the results indicate the same trend established in Ref. 2 of a higher pressurization rate producing a larger effect. These results are presented for the condition which includes thermoelastic coupling. However, the omission of the thermoelastic coupling produced no significant differences. The results show that the dynamic burning rate approaches the steady state burning rate very rapidly and at 50 milliseconds there is less than 4 percent difference for both pressurization rates. The pressure-time history for both loading conditions is also shown in Fig. V-3.

Influence on Propellant Burn Rate Produced by Oscillating Pressure Loads

The propellant burning rate is directly proportional to the pressure in the combustion chamber; hence, if the combustion chamber pressure oscillates, the propellant burn rate also oscillates. Perturbation and/or oscillation of the combustion chamber pressure may be produced from many sources. A few sources of particular interest are wave motion in the combustion chamber during ignition or rapid thrust termination, irregular and possibly unstable burning, motor and/or vehicle vibrations and in the case of vehicles like the Space Shuttle, vibrations produced by unsteady combustion in the liquid engines; e.g., the POGO phenomenon. The latter problem is studied in Ref. 24 and was shown to be insignificant with regard to the Space Shuttle propellant. The effect of motor and vehicle vibrations is discussed in a later portion of this section. For the present we consider oscillations in combustion pressure such as might be produced by a series of equal amplitude pressure waves moving across the surface. The pressure oscillations are represented by functions of the following form:

$$P = c_1 P_{av} \sin \omega t + P_{av} \quad (V-4)$$

where P_{av} is the average pressure and c_1 and ω are arbitrary constants.

This pressure function was incorporated into the thermoelastic computer program as the driving mechanical load with P_{av} , ω and c_1 being used as variables. Samples of the results obtained are shown in Figs. V-4 through V-6.

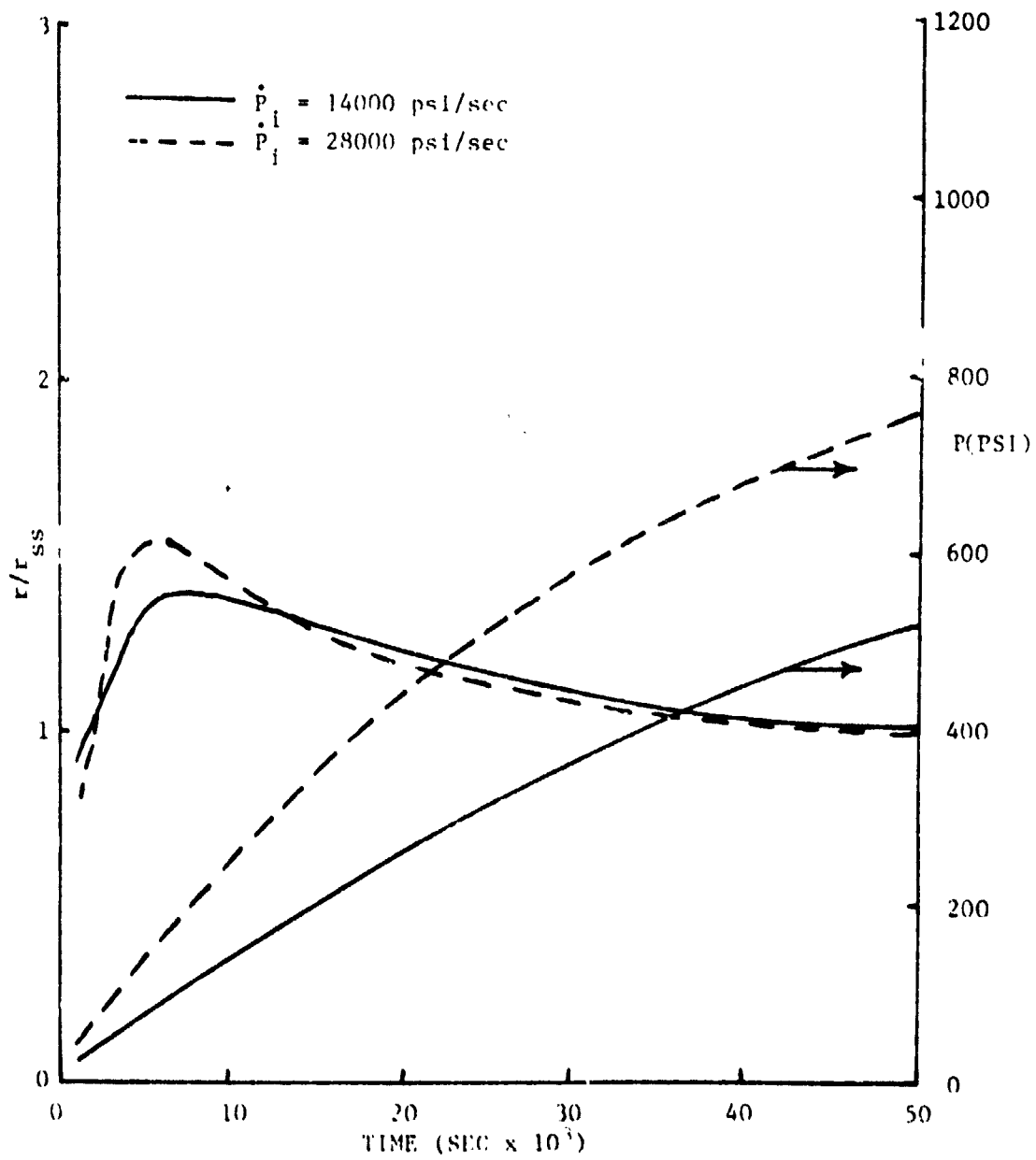


Figure V-1. Comparison of the results obtained for different pressurization rates.

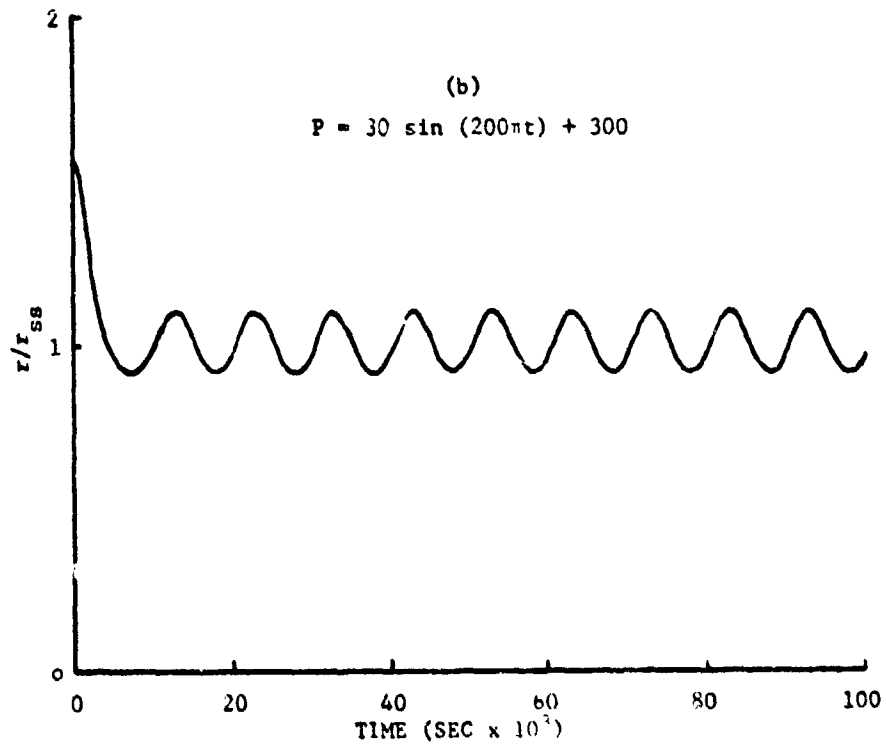
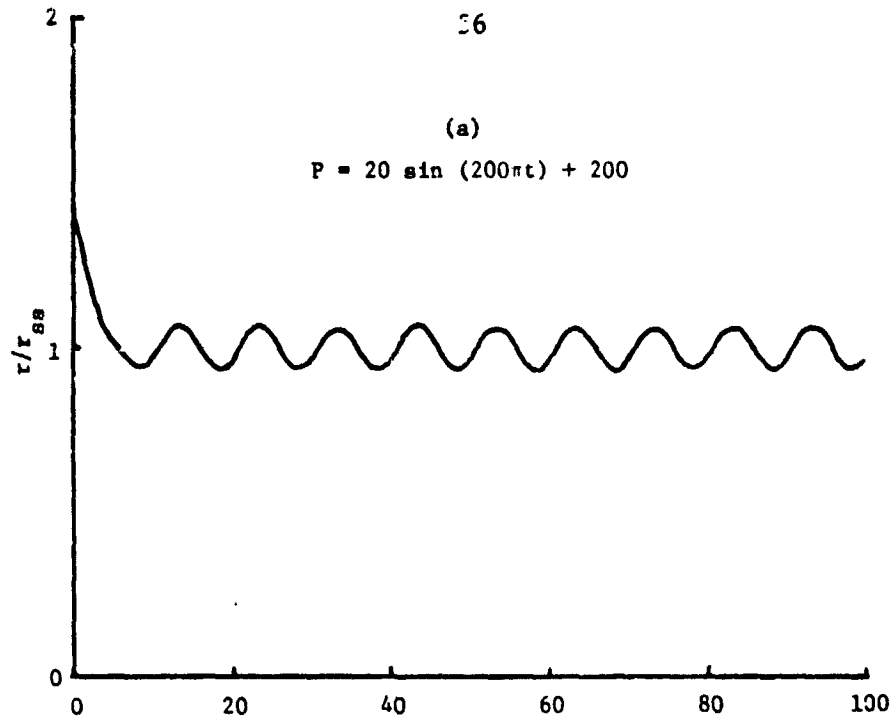


Figure V-4. Results obtained for two oscillating pressure loads ($P_{av} = 200$ and 300 psia).

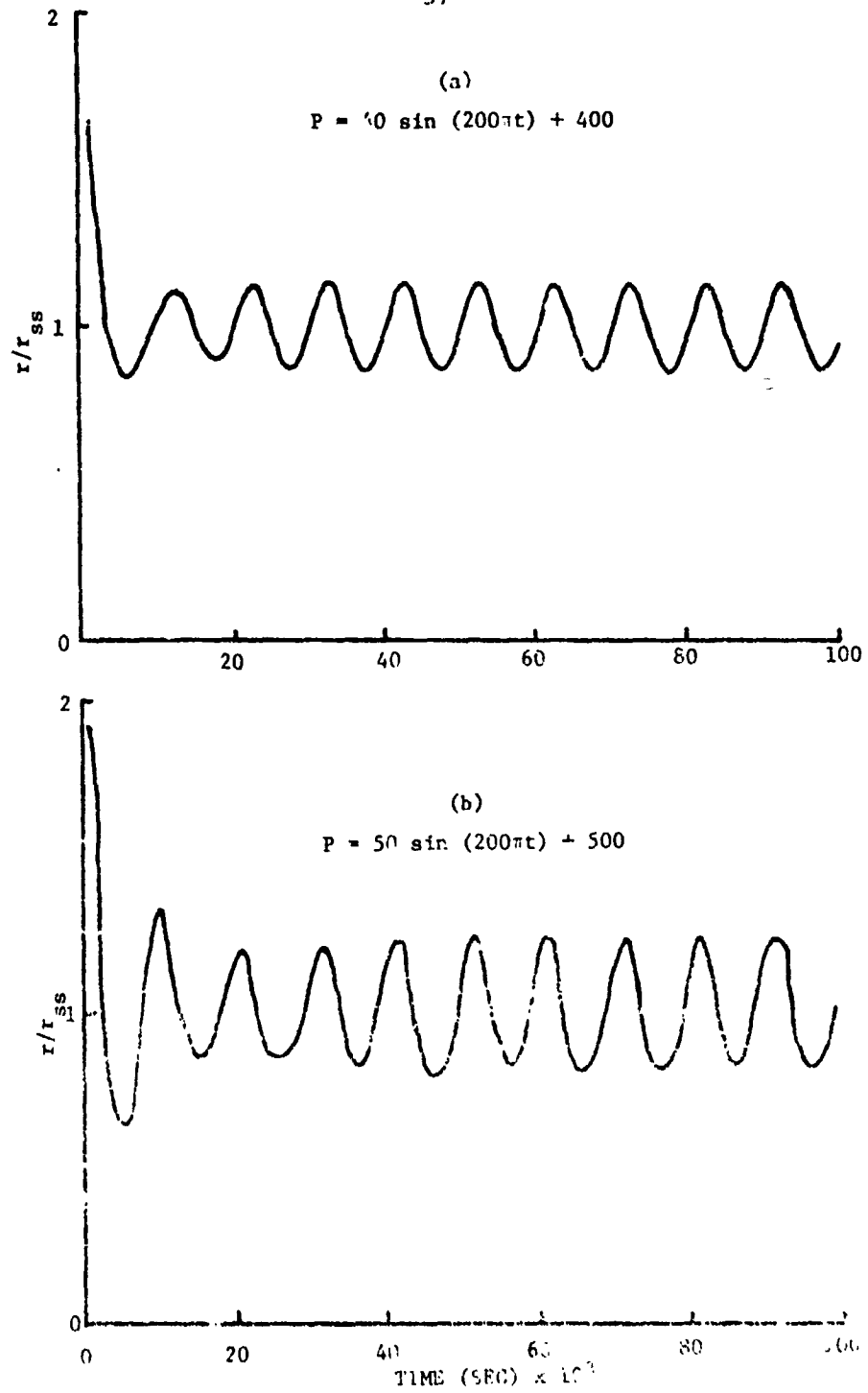


Figure V-5. Results obtained for two oscillating pressure loads ($P_{av} = 400$ and 500 psia).

ORIGINAL PAGE IS
OF POOR QUALITY

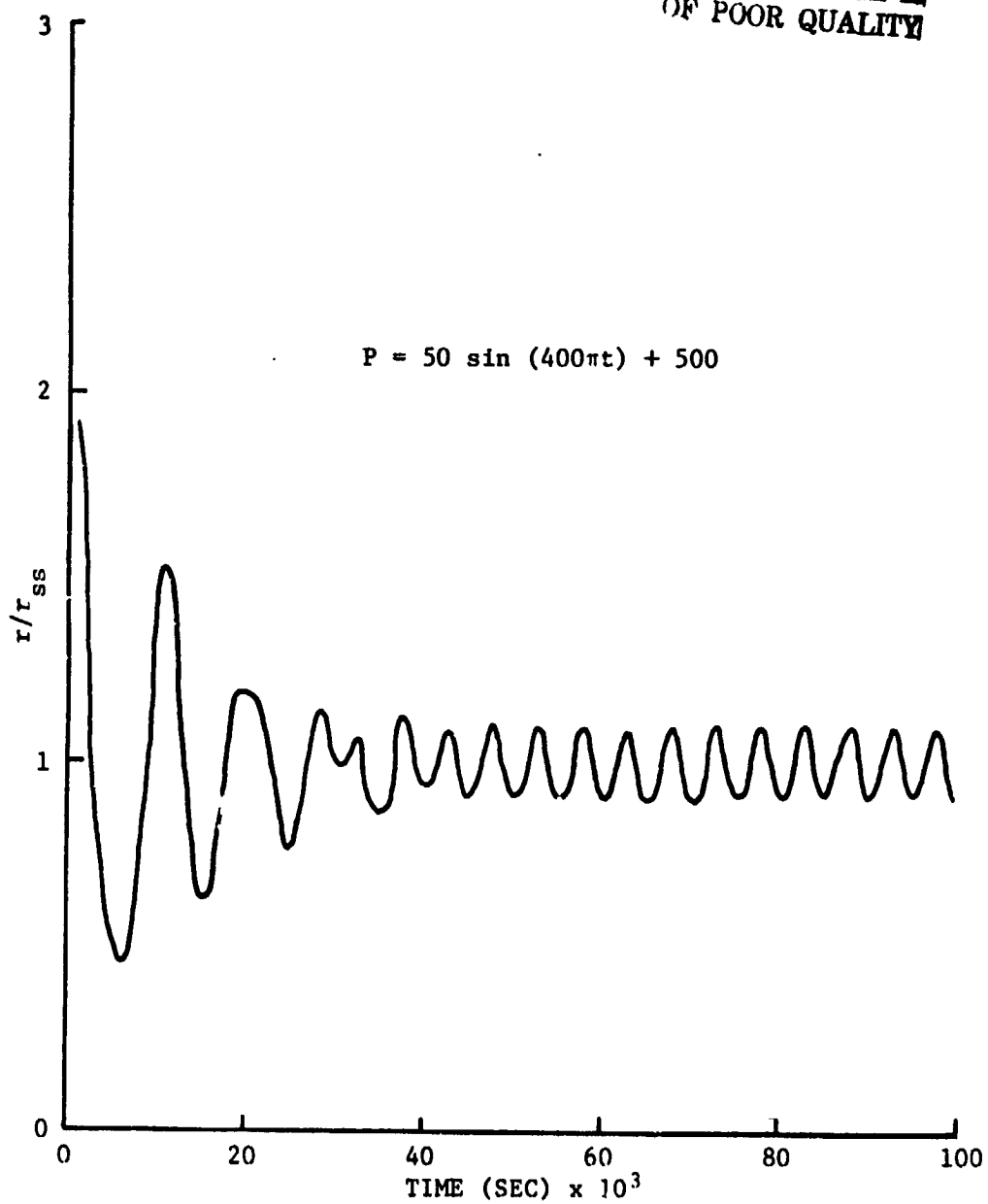


Figure V-6. Results obtained for oscillating pressure load
($P_{av} = 500$ psia).

Figures V-4 and V-5 show the results for values of P_{av} ranging from 200 to 500 psi with $\omega = 200\pi$ rad/sec and $C_1 = 0.10$. These results again show that only a negligible effect is produced by thermoelastic coupling and hence only one curve, that which includes thermoelastic coupling, is shown. The ratio r/r_{ss} is plotted versus time and the curves indicate a general tendency for this ratio to oscillate at a relatively small constant amplitude at low pressures but at higher pressures there appears to be a tendency for the oscillations to initially be relatively large and then to decay. The oscillations have a period equal to the period of the pressure oscillations but are shifted slightly in phase. Possible causes for the phase shift may be the finite time required for the propellant to respond to the pressure loading or the finite time step used in the numerical calculations; however, neither explanation has been verified.

Figure V-6 shows the results obtained when the frequency for the loading condition of Fig. V-5b is doubled. This was done to amplify the thermoelastic coupling. However, the results indicate the thermoelastic coupling is still negligible and the tendency for the oscillations to damp is still present. The reason(s) for the obvious change in frequency of the curve shown in Fig. V-6 are not presently understood.

In summary, the oscillating pressure load showed no tendency to enhance the effect of thermoelastic coupling phenomena. Therefore, it must be concluded that even though thermoelastic coupling does exist and can be modeled at least in an approximate way, there appears to be no advantage in considering its effect on the burning rate of solid propellants under the loading conditions analyzed in this work and in Ref. 2.

Effects of Poisson's Ratio, Thermal Expansion and Thermal Conductivity

In addition to the propellant modulus the energy equation for the coupled thermoelastic problem,

$$\frac{\partial T}{\partial t} = r(t)\partial T/\partial x + (\lambda/\zeta c) \nabla^2 T - T\alpha E\dot{\epsilon}/[\rho c(1-2\nu)] \quad (V-5)$$

contains terms involving other material properties. Three of these are Poisson's ratio, ν , coefficient of thermal expansion, α , and coefficient of thermal conductivity, λ . The propellant density, ρ , and specific heat at constant volume, c , also appear but are subject to less variation than the other three.

The thermoelastic dissipation term, D ,

$$D = T\alpha E\dot{\epsilon}/[\rho c(1-2\nu)] \quad (V-6)$$

varies inversely with Poisson's ratio. For a typical solid propellant, Poisson's ratio is of the order of 0.499. With this value the term $(1-2\nu)$ in the denominator is 0.002. For a Poisson's ratio of say 0.4, the term $(1-2\nu)$ becomes 0.2. Therefore, a change of approximately 25 percent in Poisson's ratio changes a factor in the denominator by two orders of magnitude. Hence, the already small dissipation term becomes negligible with the smaller Poisson's ratio. It is necessary to conclude that reducing Poisson's ratio with all other factors unchanged essentially eliminates the thermoelastic coupling. By the same token, increasing Poisson's ratio to say .4999 will increase the coupling by an order of magnitude. Figure V-7 shows the results obtained for values of Poisson's ratio of .499 and .4999. Values for smaller Poisson's ratio approximate closely the uncoupled solution which has already been shown to be unimportant. Again, only small changes result when the value of Poisson's ratio is changed.

The remaining two material properties, coefficients of thermal conductivity and thermal expansion were varied individually. The results obtained from this parametric analysis are shown in Figs. V-8 and V-9.

Figure V-8 shows the resulting r/r_{ss} ratio for values of the coefficient of thermal expansion of 0.1×10^{-3} and $0.1 \times 10^{-4}/^{\circ}\text{R}$. Only small changes in amplitude exist between the two cases with no apparent phase shift in the time-dependent response. Note also that the amplitude of r/r_{ss} is essentially the same as that shown in Fig. V-5b using the nominal value for the coefficient of thermal expansion. Hence, it appears that variations in the coefficient of thermal expansion will produce only small changes in the dynamic burning rate. It should also be pointed out that the results shown in Fig. V-8 include thermoelastic coupling, but no significant effects were noted due to the coupling.

Figure V-9 shows r/r_{ss} values for coefficients of thermal conductivity of 5.1×10^{-5} and 5.1×10^{-7} BTU/sec-in.- $^{\circ}\text{R}$.

In these results there is a significant change in amplitude as well as a phase shift produced by varying the thermal conductivity. The lower thermal conductivity produces smaller amplitudes of r/r_{ss} which means that the dynamic burning rate is closer to the steady state rate than the dynamic burning rate for the higher coefficient of thermal conductivity. There is also a phase shift between the two curves due to the lower thermal conductivity slowing down the heat transfer process. This is evident since the pressure loadings in each case were in phase, yet the peak amplitudes for the case of the lower coefficient of thermal conductivity occur at later times. Again, no significant influence of thermoelastic coupling was noted.

In summary, the results obtained from varying the propellant properties show that the propellant burning rate has a small variation with respect to these material properties. The burning rate variations produced by

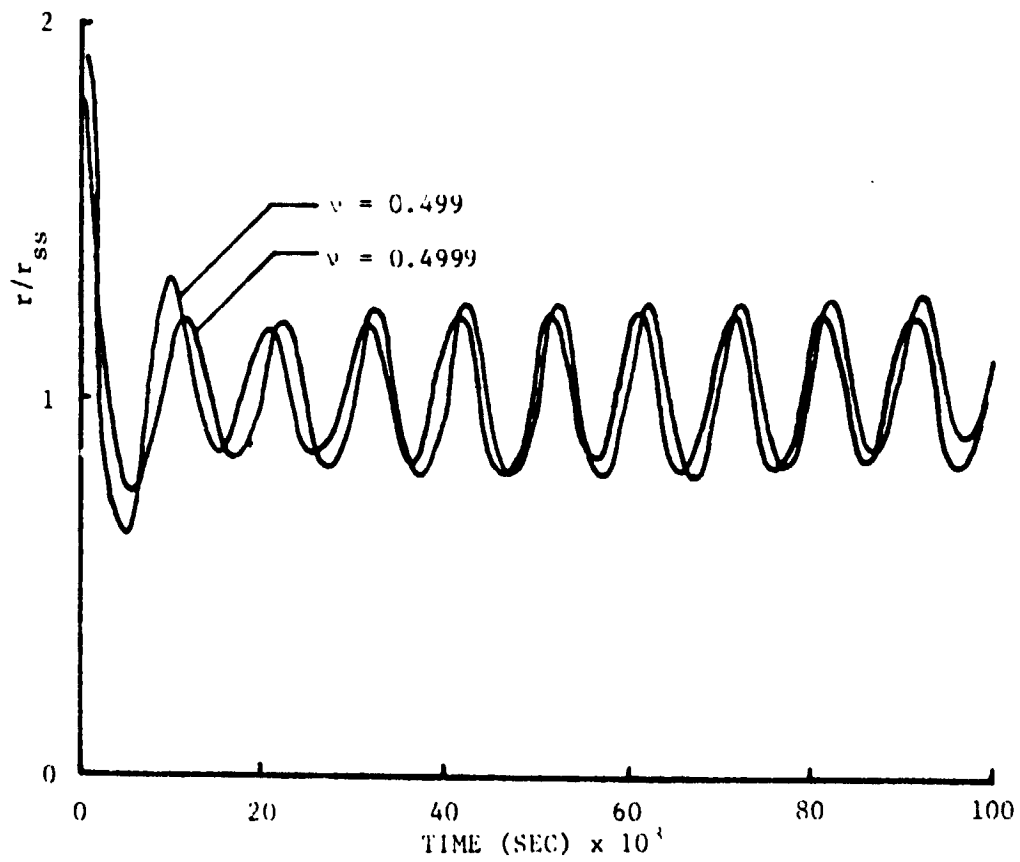


Figure V-7. Comparison of results obtained for two values of Poisson's ratio (Pressure = $50 \sin (200\pi t) + 500$).

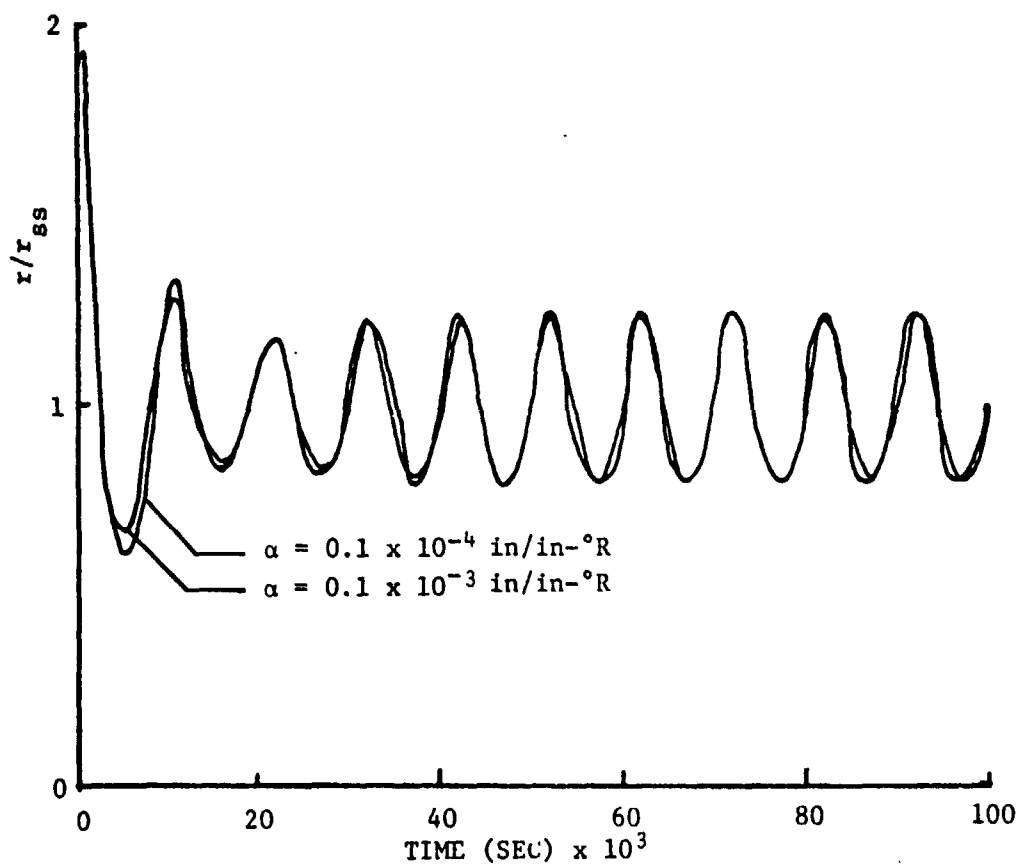


Figure V-8. Comparison of results obtained for two values of coefficients of thermal expansion.
(Pressure = $50 \sin(200\pi t) + 500$)

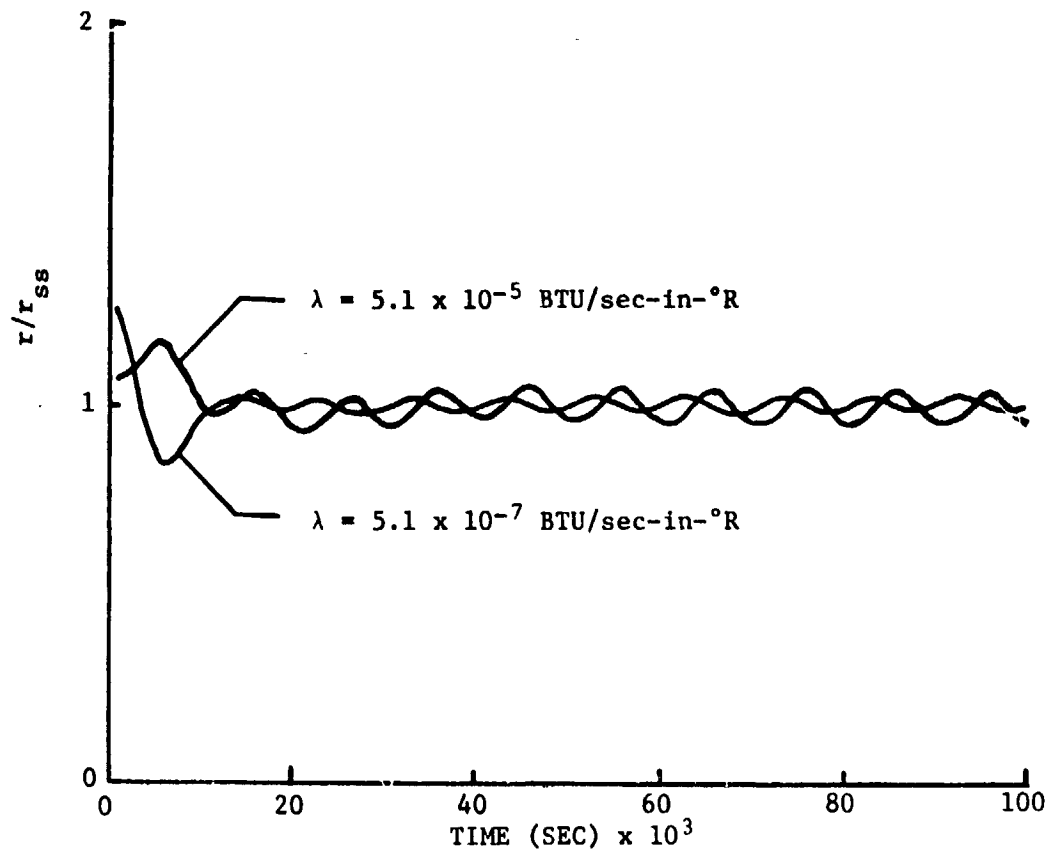


Figure V-9. Comparison of results obtained for two different coefficients of thermal conductivity.
(Pressure = $50 \sin(200\pi t) + 500$)

changing Poisson's ratio and the coefficient thermal expansion are indicative of modifications made to the thermoelastic dissipation term of Eq. V-5, since they only appear in this term. This is also true for changes in the propellant modulus discussed earlier. The burning rate variations due to changes in thermal conductivity do not directly indicate the influence of thermoelastic coupling since the conductivity does not appear in the dissipation term of Eq. V-5.

Effects of Mechanical Vibration on Motor Performance

Mechanical vibrations in the propellant of an SRM produce temperature changes in the propellant due to viscous dissipation of mechanical energy as well as from volumetric changes associated with the thermoelastic effect. The previous subsection has shown that the thermoelastic effect is negligible and it will be neglected in this portion of the work.

A vibration analysis of a Space Shuttle type SRM is presented in Ref. 25. The analysis in Ref. 25 uses the results of Ref. 26 to determine the temperature change in the propellant per cycle of oscillation.

For an element of propellant undergoing a pure shear vibration, the temperature change per cycle of oscillation determined in Ref. 26 is

$$\Delta T = \pi \beta |\tau|^2 / G' \rho c \quad (V-7)$$

where ΔT is the temperature change per cycle, β is the shear loss modulus, G' is the real part of the complex shear modulus at a given frequency of oscillation, ρ is the propellant density, c is the specific heat at constant volume and τ is the peak value of the oscillatory shear stress.

Reference 26 also gives the temperature change per cycle of oscillation for a uniaxial stress oscillation as

$$\Delta T = 3\pi \bar{\beta} |\sigma|^2 / 4E' \rho c \quad (V-8)$$

where $\bar{\beta}$ is the tensile loss modulus, E' is the real part of the complex tensile modulus and σ is the peak value of the oscillatory normal stress.

For a typical propellant we have from Ref. 24:

$$\beta = \bar{\beta} = 0.4$$

$$E' = 3000 \text{ psi}$$

$$G' = 1000 \text{ psi}$$

$$\rho c = 160 \text{ lbf/in}^2/\text{°R}$$

These values give:

$$\Delta T_{\text{shear}} = 8 \times 10^{-6} |\tau|^2$$

$$\Delta T_{\text{uniaxial}} = 2 \times 10^{-6} |\sigma|^2$$

Since the temperature change due to shear oscillations is larger, we conservatively assume that it holds for any vibrational mode. Reference 25 gives 10 psi as a moderate to large oscillatory stress magnitude. Using this stress magnitude, Eq. V-7 predicts that the change in temperature per cycle of oscillation is 0.0008°R . Reference 25 also points out that experimental results from a vibration test of a Sparrow motor at Allegany Ballistics Laboratory indicated a 10°R change after 30 minutes of vibration testing. The amplitude and frequency of the vibration test were not readily available and obviously the Space Shuttle SRM and the Sparrow motor are not of the same size class. But, if one makes the assumption that the Sparrow tests are indicative of the magnitude of the temperature changes one could expect from a Space Shuttle SRM the value of $0.0008^\circ\text{R}/\text{cycle}$ would be considered a conservative estimate. With these limitations an analysis was made to determine the influence on performance of a Space Shuttle type SRM subjected to a vibrational environment which produced a $0.0008^\circ\text{R}/\text{cycle}$ change in grain temperature. The motor was assumed to vibrate with a stress amplitude of 10 psi at frequencies of 15 and 75 Hz. These frequencies are representative of the fundamental vibrational frequency of the vehicle and of its 5th harmonic. The results from this analysis for motor thrust versus time are shown in Fig. V-10 compared to the case of no vibration. Virtually no difference in performance is noted between the no-vibration analysis and the 15 Hz analysis. A small difference between the no-vibration and the 75 Hz analyses is shown to exist. It is interesting to note that these differences occur immediately preceding star grain burn out (≈ 20 sec), during the time of maximum dynamic pressure (≈ 60 sec), and during tailoff. By itself the vibration problem poses no real problem with regard to motor performance. However, due to the occurrence at these three critical times during the motor's operation, there exists a possibility, however small, of the enhancement by vibration of other performance variations to the point at which the combined effect could be important. The percent differences produced by mechanical vibration in web time were 0.11 and 0.56 percent for the vibrational frequencies of 15 and

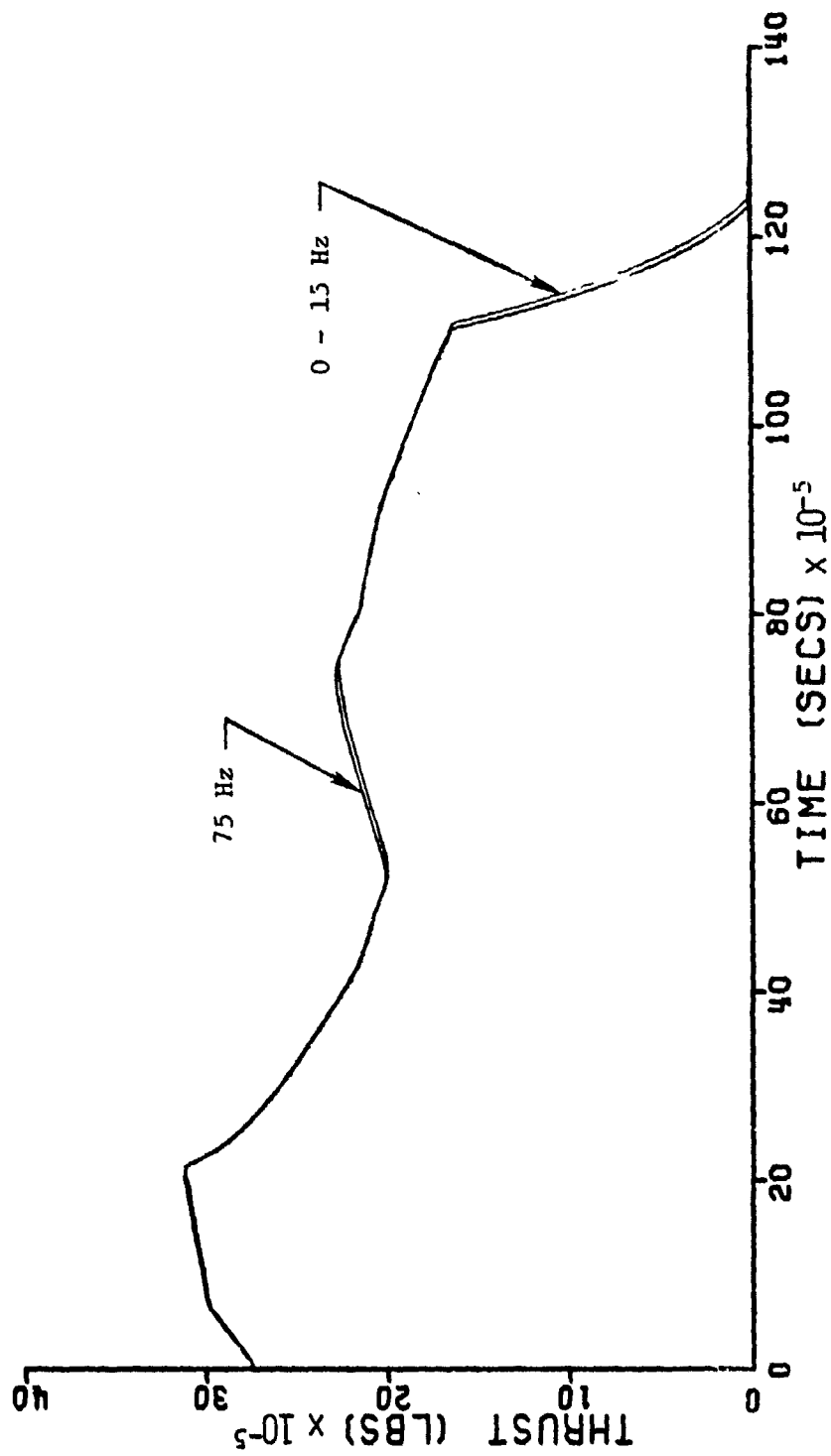


Figure V-10. Thrust versus time curves for various vibrational frequencies.

75 Hz, respectively. The change in burning rate at web time was 0.19 and 0.98 percent for the 15 and 75 Hz frequencies, respectively. The maximum head end pressure changed 0.05 and 0.23 percent and the average nozzle stagnation pressure changed 0.14 and 0.74 percent for the 15 and 75 Hz frequencies, respectively.

The results of this analysis indicate that the mechanical vibrations of the amplitude and frequency, 10 psi and 15 Hz, expected for a Space Shuttle type SRM would produce negligibly small effects on performance. However, it should be noted that larger amplitudes and/or frequencies of vibration tend to produce more significant effects on SRM performance and should be accounted for if they are found to exist.

Summary of Ignition Transient Analysis

During the course of this investigation an internal ballistics model of the ignition transient was developed using the Z-N burning rate model and incorporating the thermoelastic analysis. This was done so as to better represent the ignition transient than is possible by assigning a pure exponential pressure loading. Although the thermoelastic effect, which has now been shown to be small, is not augmented significantly by such treatment, the Z-N analysis may prove of some utility. Generally, the method is an adaptation of the ignition analysis technique presented in Refs. 6 and 27, but with the Z-N burning rate model (and, initially, the thermoelastic coupling) included. The major work on the analysis was performed as a separate effort as a graduate thesis under guidance of this project and details will be presented in Ref. 8. Only a brief description and illustration of the results is given here.

The determination was made early in the analysis that the thermoelastic coupling has much less effect on the ignition transient prediction than does the unsteady Z-N burning rate. And since the thermoelastic coupling analysis needlessly adds to the computer time and storage requirements, it is not considered in the analysis of Ref. 8. The analysis compares predicted ignition transients incorporating the unsteady Z-N burning rate law to predictions using the classical Vieille burning rate law ($r = aP^n$) and to test data for the Titan IIIC and Space Shuttle SRMs. The propellant properties necessary for the Vieille ignition transient are well known, but the propellant constants in the Arrhenius burning rate law, necessary for the Z-N formulation, are not so well known. Also, the flame-spreading speed is uncertain. Following the procedure of Ref. 8, these unknown quantities are adjusted to establish a good fit of the Z-N ignition thrust transient to the Titan IIIC test data. The flame-spreading speed is adjusted so that the maximum rate of thrust rise for the Vieille ignition transient prediction matches the maximum rate exhibited by the Titan IIIC test data. This value of flame-spreading speed (4300 ft/sec) is then used throughout all analyses. The Arrhenius constants are then adjusted to produce a good fit of peak thrust of the Titan IIIC ignition

transient test data. In the absence of any better information, the same values of Arrhenius pre-exponential factor (740 in/sec), activation energy (4900 cal/gmole), and flame-spreading speed are used in the ignition transient prediction of the Space Shuttle SRM.

Using these propellant constants, the Z-N and Vieille ignition transient predictions are calculated for the Space Shuttle SRM and compared in Fig. V-11 to test data from Ref. 19. It is immediately perceived that both predictions exhibit a much smaller rate of pressure rise than the test data, thus underestimating the pressure throughout the transient. However, the Z-N model does exhibit a slightly higher rate of pressure rise than the Vieille model, and more closely predicts the pressure during the latter portion of the ignition transient.

It might be suspected from examination of the rate of pressure rise in Fig. V-11 that the flame-spreading speed is not of sufficient magnitude. In fact, MSFC, using a program developed by Caveny (Ref. 28), has analytically predicted a flame-spreading speed in excess of 27,000 in/sec for the Space Shuttle SRM (Ref. 29). But this analysis also gave a predicted rate of thrust rise which is approximately twice that exhibited by the test data. This might indicate that the actual flame-spreading speed is approximately half that predicted. The results of using a flame-spreading speed of 12,000 in/sec in the present Z-N analysis are given in Fig. V-12. The ignition transient pressure predictions are much improved, and especially the Z-N model during the latter portion of the transient. Note that the pressure differential between the Z-N and Vieille models is greater with the increased flame-spreading speed. This is a result of the increased Z-N burning rates resulting from the more rapid rate of pressure rise with increased flame-spreading speed.

Additionally, in Fig. V-12 it is noted that during the initial 200 milliseconds, the pressure is overestimated while the rate of pressure rise is underestimated. The overestimation of pressure might be attributed to the fact that no delay associated with ignition initiation is incorporated in the analysis. And the underestimation of pressure rise may be caused by the assumption that the propellant grain is ignited adjacent to the igniter and progresses with time from that point. But, in fact, the propellant is probably ignited, after a delay, for some distance down the motor port, resulting in a higher-than-predicted pressure rise during this portion of the transient. It is planned to incorporate these considerations into the analysis at a later time.

Although there exists some uncertainty of flame-spreading speed and Arrhenius burning law constants, the Z-N theory does show potential, as demonstrated in Refs. 7 and 8, for more accurately predicting the unsteady burning rates associated with ignition and extinguishment transients. The Z-N theory has been demonstrated to be functional over a wide range of Arrhenius constants, but any additional quantitative conclusions on the validity of the model must await more reliable values of the Arrhenius constants.

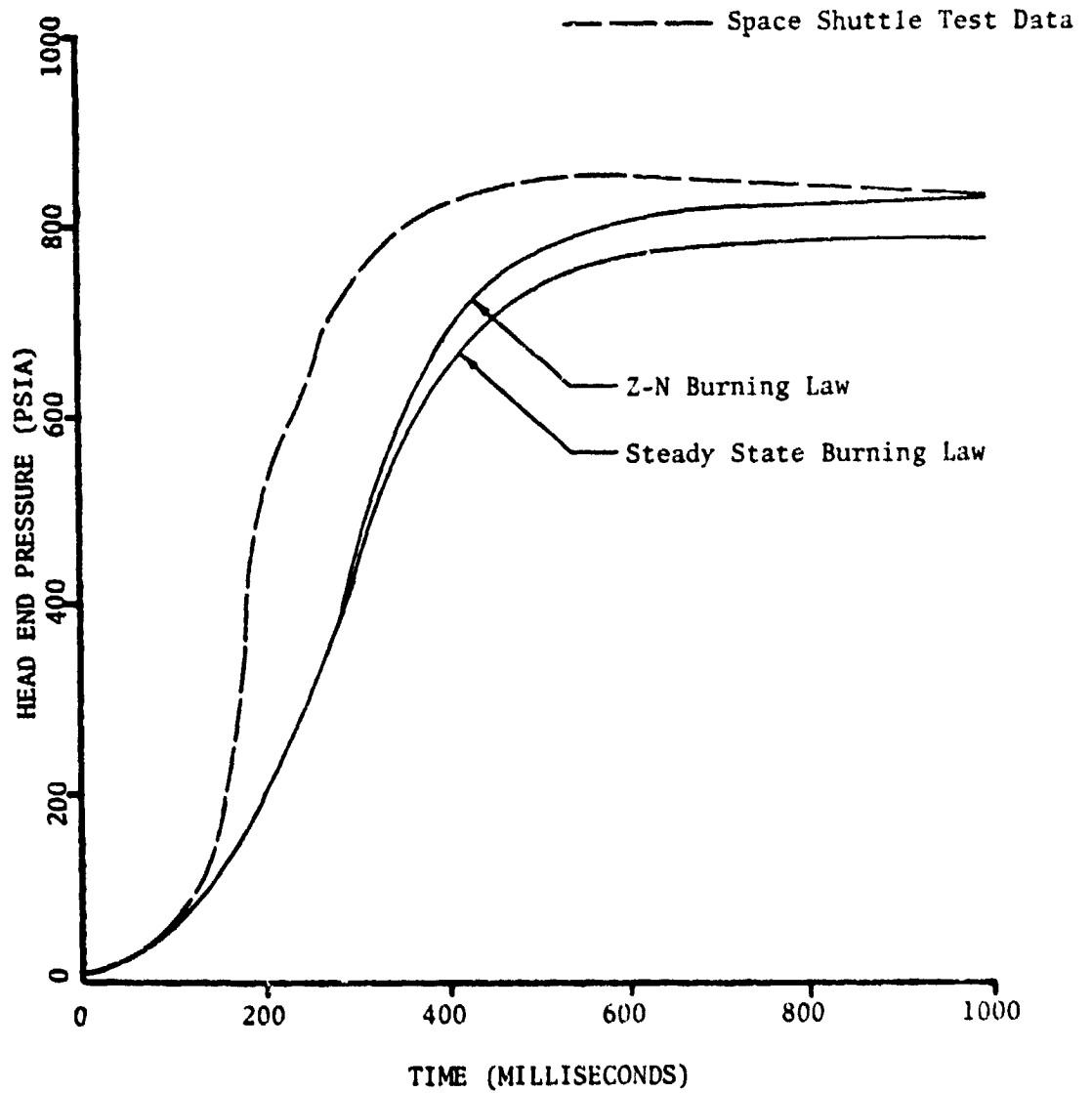


Figure V-11. Comparison of the predicted ignition transients and test data for the Space Shuttle SRM.

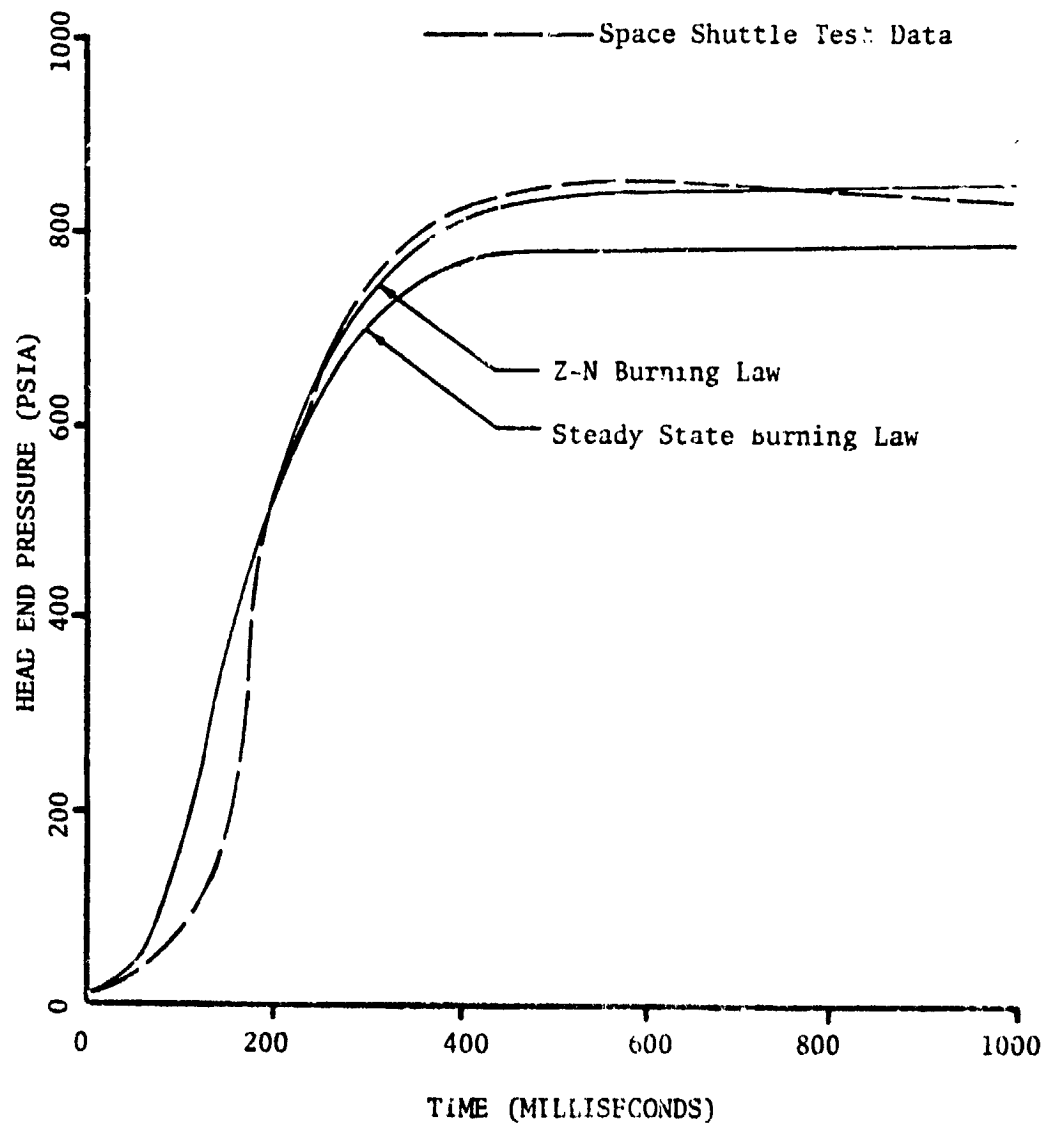


Figure V-12. Effect of increased flame-spreading speed on the predicted ignition transient for the Space Shuttle SRM.

VI. CONCLUDING REMARKS

The continued research in internal ballistic performance variation has produced considerable reduction in computer execution times for both the design analysis and Monte Carlo programs. Handling of input data by the user has been simplified and the volume of printed material reduced.

An alternative technique has been developed for predicting thrust imbalance without recourse to the Monte Carlo program which is best applied to the tailoff portion of the operation. A scaling relationship has been established to relate theoretical results to test results which may be applied to the alternative technique of predicting thrust imbalance or to the Monte Carlo evaluation.

Additional evidence of the validity of the analysis of circular-perforated propellant deformation effects upon internal ballistic performance has been presented. The grain deformation analysis coupled with a new model of erosive burning seems to offer great potential for improving the predictability of SRM performance. The technique, however, needs to be further investigated before the approach is incorporated into the Monte Carlo program. Particular attention needs to be given to two-dimensional nozzle flow and erosive burning threshold velocity effects. Although we have presented an approach for extending the grain deformation analysis to star-type grains, the method is somewhat cumbersome. The framework has been set, however, for a simplified approach. The more rigorous approach has also shown star grain deformation would be of small consequence for many configurations, e.g., the Space Shuttle.

Finally, the extended investigation into the effect of strain rate on propellant burning rate leads to the conclusion that the thermoelastic effect is generally negligible for both steadily increasing pressure loads and oscillatory loads. No reason appears to exist for continued research in thermoelastic behavior. However, the capability to calculate the influence of oscillating pressure loads on transient burning rates making use of the Zeldovich and Novozhilov transient burning rate model may prove useful in combustion instability investigations.

REFERENCES

1. Sforzini, R. H., and Foster, W. A., Jr., "Monte Carlo Investigation of Thrust Imbalance of Solid Rocket Motor Pairs," Journal of Spacecraft and Rockets, Vol. 13, No. 14, April 1976, pp. 198-202.
2. Sforzini, R. H., and Foster, W. A., Jr., "Solid-Propellant Rocket Motor Ballistic Performance Variation Analyses (Phase Two)", Final Report, NASA Contractor Report CR-150324, Auburn University, September 1976.
3. Sforzini, R. H., and Foster, W. A., Jr., "Solid-Propellant Rocket Motor Ballistic Performance Variation Analyses," Final Report, NASA Contractor Report CR-144264, Auburn University, September 1975.
4. Sforzini, R. H., Foster, W. A., Jr., and Johnson, F. S., Jr., "A Monte Carlo Investigation of Thrust Imbalance of Solid Rocket Motor Pairs," Final Report, NASA Contractor Report CR-210700, Auburn University, November 1974.
5. Sforzini, R. H., "Design and Performance Analysis of Solid-Propellant Rocket Motors Using a Simplified Computer Program," Final Report, NASA Contractor Report CR-129025, Auburn University, October 1972.
6. Sforzini, R. H., "Extension of a Simplified Computer Program for Analysis of Solid-Propellant Rocket Motors," Final Report, NASA Contractor Report No. CR-129024, Auburn University, April 1973.
7. Summerfield, M., Caveny, L. H., et al, "Theory of Dynamic Extinguishment of Solid Propellants with Special Reference to Nonsteady Heat Feedback Law," AIAA Journal, Vol. 8, No. 3, March 1971, pp. 251-258.
8. Murph, Jesse E., "Prediction of Ignition Transients in Solid Rocket Motors Using a Nonsteady Heat Feedback Law," Master of Science Thesis, Auburn University, December 8, 1977.
9. Smith, D. F., "Solid-Propellant General Deformations and Their Effect on Motor Performance," Master of Science Thesis, Auburn University, December 1976.
10. Nelson, G. R., and Baker, J. S., "Burn-Rate Anomaly Rate Factor (BARF) Large Motor Study," Final Report, Thiokol Corporation, Wasatch Division, Brigham City, Utah, June 1976.
11. Shapiro, A. H., The Dynamics and Thermodynamics of Compressible Fluid Flow, Vol. 1, The Ronald Press, New York, 1953, p. 239.

REFERENCES (Continued)

12. "Final Test Report, TU-455.02 Rocket Motor Submerged Gimbal Nozzle," Thiokol Chemical Corporation, Wasatch Division, Brigham City, Utah, October 5, 1965.
13. "156-Inch Diameter Motor Jet Tab TVC Program, Test Results, First 156-Inch Diameter Motor," Lockheed Propulsion Company, Redlands, California, June 27, 1964.
14. "260-Inch Diameter Motor Feasibility Demonstration Program, Static Test Firing of Motor 260-SL-1," Final Report, NASA Contractor Report No. CR-54865, Aerojet General Corporation, Sacramento, California, October 25, 1965.
15. "260-Inch Diameter Motor Feasibility Demonstration Program, Static Test Firing of Motor 260-SL-2," Final Report, NASA Contractor Report No. CR-54982, Aerojet General Corporation, Sacramento, California, March 25, 1966.
16. "Final Test Results of the 156-2C-1 Motor Firing," Report No. SBR84,565, NASA Contract No. NAS3-6285, Thiokol Chemical Corporation, Space Booster Division, Brunswick, Georgia, May 14, 1965.
17. "Technical Description of the TX 354-5 Rocket Motor," Huntsville Division, Thiokol Chemical Corporation, Control No. U-67-1005A, May 9, 1967.
18. Williams, F. A., Barrère, M., and Huang, N. C., Fundamental Aspects of Solid Propellant Rockets, Technivision Services, Slough, England, 1969, pp. 381-382, 401-446.
19. "Development Motor No. 1, Flash Report for Space Shuttle Rocket Motor Project," TWR-11517, Ref. A, NASA Contract NAS8-30490, Thiokol Corporation, Wasatch Division, Brigham City, Utah, July 20, 1977.
20. Becker, E. B., and Brisbane, J. J., "Application of the Finite Element Method to Stress Analysis of Solid Propellant Rocket Grains," Report No. S-76, Vol. II, Part 2, Rohm & Haas Company, Redstone Arsenal Research Division, Huntsville, Alabama, January 21, 1966.
21. Williams, M. L., Blatz, P. J., and Schapery, R. A., "Fundamental Studies Relating to System Analysis of Solid Propellants," Graduate Aeronautical Laboratory, California Institute of Technology, SM61-5, February 1961, p. 38.

REFERENCES (Concluded)

22. Williams, M. L., Landel, R. F., and Ferry, J. D., "The Temperature Dependence of Relaxation Mechanisms in Amorphous Polymers and Other Glass-Forming Liquids," J. Am. Chem. Soc., Vol. 77, July 1955, pp. 3701-3707.
23. Kruse, R. B., Unpublished Data, June 1963.
24. Culick, F. E. C., "Coupling Between Pressure Oscillations in the SRB and POGO Instability," Memorandum to MSFC, California Institute of Technology, September 1976.
25. Anderson, J. M., and Beckstead, M. W., "An Evaluation of Acoustic Driving Through Grain Vibration Heating," Memorandum to MSFC, Hercules Incorporated, March 1976.
26. Schapery, R. A., "Effect of Cyclic Loading on the Temperature in Viscoelastic Media with Variable Properties," AIAA Journal, Vol. 2, No. 5, May 1964, pp. 827-835.
27. Sforzini, R. H., and Fellows, H. L., Jr., "Prediction of Ignition Transients in Solid-Propellant Rocket Motors," Journal of Spacecraft and Rockets, Vol. 7, No. 5, May 1970, pp. 626-628.
28. Cavany, L. H., and Kuo, S. K., "Ignition Transients of Large Segmented Solid Rocket Boosters," Final Report NASA Contractor Report No. CR-150162, Princeton University, April 1976.
29. Shackelford, B. W., Informal communication from NASA to the authors, October 1977.